

# Analysis of Avalanche Runaway Generation after Disruptions with Low- $Z$ and Noble Gas Species<sup>\*)</sup>

Akinobu MATSUYAMA and Masatoshi YAGI

*National Institutes for Quantum and Radiological Science and Technology, Rokkasho, Aomori 039-3212, Japan*

(Received 22 February 2017 / Accepted 26 June 2017)

The effects of impurities on runaway electron generation are studied using a zero-dimensional disruption simulation code. For describing collisions between fast electrons and partially stripped ions, a charge-resolved expression of the Coulomb logarithm is employed. Numerical analysis of the avalanche growth rate using the adjoint Fokker-Planck method is compared with two existing semi-analytic models, showing (i) the convergence of the growth rate to strong electric field limit of the Rosenbluth-Putvinski (R-P) model and (ii) the cancellation of the effect of second-order collisional diffusion for intermediate electric fields. Using the developed current quench (CQ) simulations, the parametric study is performed with the aid of the power balance analysis, which characterizes the onset of strong avalanche amplification in the presence of low- $Z$  and noble gas species. Thermal quench (TQ) simulations are also developed for self-consistent evaluation of hot-tail seed electrons. The deposition timescale of impurity neutrals is shown to have significant impacts on hot-tail seeds, depending non-monotonically on the pre-TQ temperature and the injected impurity density.

© 2017 The Japan Society of Plasma Science and Nuclear Fusion Research

Keywords: runaway electron, disruption, massive gas injection, radiation, ITER

DOI: 10.1585/pfr.12.1403032

## 1. Introduction

To present, the development of disruption mitigation methods has been progressed towards operation of ITER, which is aimed at minimizing heat and electromagnetic loads within acceptable levels [1–3]. Nevertheless, reliable mitigation of runaway electrons (REs) is still an active area of research. With high plasma current on the order of 10 MA, the avalanche mechanism due to close collisions [4, 5] is predicted to dominate the RE generation in ITER [6], which may cause severe damages to the in-vessel components.

To predict the RE currents produced in post-disruption plasmas, high impurity content is a key characteristic. Firstly, radiation losses affect the plasma parameter during thermal quenches (TQ). After TQ, the power balance between ohmic heating and radiation loss dominates the current quench (CQ) time and one-turn voltages that accelerate runaway electrons. While CQ in the metallic wall environment with a relatively low radiation such as JET-ILW [7] is observed to be slow enough to avoid runaway generation, the massive impurity injection to mitigate thermal loads shortens the CQ time, which results in runaway generation [8]. Secondly, impurities dominate the runaway generation rate. The net friction force acting on the electrons is enhanced by partially stripped ions at low electron temperature. The so-called Rosenbluth density  $n_{RB}$  [9] characterizes a value of the electron density necessary for

absolute suppression by means of massive impurity injection. Thirdly, primary (seed) runaways required for triggering the avalanche growth are sensitive to dynamic changes of the plasma parameters during TQ. At the high density conditions, hot-tail seeds [10–18] can be a dominant mechanism when the Dreicer seed electrons are suppressed. For the development of rapid shutdown scenarios using massive noble-gas injection, the production of hot-tail seed electrons during rapid TQ must be taken into account.

To analyze the above three processes, we develop a zero-dimensional disruption simulation code INDEX (Integrated Numerical Disruption EXperiment). This paper describes its model verification. To capture the effects of impurities on runaway generation [19–23], the INDEX code employs an impurity collision model based on a charge-resolved expression for the Coulomb logarithm, modifying Mosher [24] with the quantum mechanical correction and the effect of plasma wave excitation. The impurity collision model is applied to two existing semi-analytic approaches calculating the critical energy and the energy limit: one is based on approximate solutions of the Fokker-Planck equation [25], and the other is based on the mean-particle equation [26]. By using identical synchrotron and bremsstrahlung radiation terms, a difference between the two models is whether second-order collisional diffusion terms are retained or not. The avalanche growth rate obtained from the above two models is compared with numerical solutions of the adjoint Fokker-Planck method [27–30]. It shows (i) the convergence of the growth rate to strong electric field limit of the

author's e-mail: matsuyama.akinobu@qst.go.jp

<sup>\*)</sup> This article is based on the invited talk on the 33rd JSPF Annual Meeting (2016, Tohoku).

Rosenbluth-Putvinski (R-P) model [6] and (ii) the cancellation of the effect of the collisional diffusion. For intermediate electric fields between the sustainment field and the strong electric field limit, the latter effect results in the growth rate even exceeding the R-P model. It is shown that the effect becomes quantitatively important at high  $Z$  and low synchrotron radiation condition.

In this paper, while paying attention to quantitative impact of differences in the avalanche models, the developed 0D CQ simulation is applied to study the amount of low- $Z$  and noble gas species required for the onset of strong avalanche amplification of small seed currents. It is shown that the avalanche growth dominates runaway generation when the equilibrium point during CQ in low  $T_e$  region ( $\lesssim 10$  eV) is accessed and when the electric field reaches the level of strong electric field limit  $E_{\parallel}/E_c \approx 10^2$ . The effect of bulk ion density to avoid the high normalized electric fields is also addressed. The above analysis based on given seed currents must be complemented by self-consistent evaluation of the seed currents. As such study, this paper also covers the development of 0D TQ simulations with the hot-tail effect. In the INDEX code, TQ is solved in terms the rate equations and the energy balance equations without assuming the ionization equilibrium. The developed TQ model is coupled self-consistently to the initial value Fokker-Planck code for evaluating hot-tail seed electrons. Some examples of the application to argon injection are illustrated, showing that the deposition timescale of impurity neutrals has significant impacts on hot-tail seed formation.

This paper is organized as follows. In Sec. 2, the problem of calculating the avalanche growth rate is reviewed for describing a main part of the calculation in the INDEX code. The fact that the avalanche theory requires the accuracy up to  $O(1/\ln \Lambda)$  is emphasized, where  $\ln \Lambda$  is the Coulomb logarithm. A charge-resolved expression of the Coulomb logarithm is described in Sec. 3. In Sec. 4, the Fokker-Planck and mean-particle approaches for calculating the critical energy and the energy limit are described, and the benchmark of the resultant avalanche growth rate against the adjoint Fokker-Planck code is presented. Section 5 is devoted to 0D CQ simulations of the avalanche runaway generation. Section 6 describes the development of 0D TQ simulations with the hot-tail effect. The conclusion and future extension of the INDEX code will be described in Sec. 7.

## 2. Avalanche Theory for Runaway Electrons in Post-Disruption Plasmas

### 2.1 Current quench (CQ) and Rosenbluth-Putvinski model

Because the TQ and CQ timescales are normally well-separated, the avalanche growth model is often

developed to describe the current decay timescale  $\tau_{CQ} = (d \log I_p / dt)^{-1}$  after TQ. Since the plasma current is conserved during TQ, the plasma parameters at the beginning of CQ can be evaluated from the power balance between ohmic heating (calculated by the pre-disruption current) and radiation losses. Consider CQ including REs for a tokamak plasma with the major radius  $R_0$  and the area of poloidal cross section  $S = \kappa a^2$  ( $\kappa$ : the elongation;  $a$ : the minor radius). The induced voltage is described by Lenz's law,  $d\psi/dt = -2\pi R_0 E_{\parallel}$ , where  $\psi$  is the poloidal flux and  $E_{\parallel}$  is the electric field. We assume that  $L_p$  is constant with time and the Ohm's law  $E_{\parallel} = \eta(j_{\parallel} - j_{RE})$ , where  $\eta$  is the resistivity,  $j_{\parallel}$  is the total current density, and  $j_{RE}$  is the runaway current density. Because the magnetic flux is written as  $\psi = L_p I_p$  in terms of the total plasma inductance  $L_p = L_e + L_i$  ( $L_e$  and  $L_i$  are external and internal inductances, respectively), the equation for the current decay including REs is given by [31]

$$L_p \frac{dI_p}{dt} = -2\pi R_0 E_{\parallel} = -R_p (I - I_{RE}), \quad (1)$$

where  $I_p \equiv j_{\parallel} S = I_{Oh} + I_{RE}$  represents the total current with the ohmic ( $I_{Oh}$ ) and runaway ( $I_{RE}$ ) ones, and  $R_p \equiv 2\pi R_0 \eta / S$  denotes the one-turn plasma resistivity. In Eq. (1) the mutual inductance to external conductors is neglected.

A 0D version of the INDEX code solves Eq. (1) with appropriate models that describe the evolution equation of RE currents  $I_{RE}$ . By assuming that REs travel at the speed of light, runaway currents are expressed as  $I_{RE} = e n_{RE} S$ , where  $n_{RE} = \int_{p > p_c} f d^3 \mathbf{p}$  is the runaway density ( $p_c$ : the critical momentum). To provide the evolution of  $I_{RE}$ , the Rosenbluth-Putvinski (R-P) model has been used, where the avalanche growth rate  $\Gamma_{RP}$  is given by

$$\Gamma_{RP} \equiv \frac{d \log n_{RE}}{dt} = \frac{E_{\parallel}/E_c - 1}{\tau \ln \Lambda} \sqrt{\frac{\pi}{3(Z+5)}} \left( 1 - \frac{E_c}{E_{\parallel}} + \frac{4\pi(Z+1)^2}{3(Z+5)(E_{\parallel}^2/E_c^2 + 3)} \right)^{-1/2}. \quad (2)$$

In Eq. (2)  $\tau = 4\pi \epsilon_0^2 m_e^2 c^3 / (n_e e^4 \ln \Lambda)$  and  $E_c = m_e c / e \tau = n_e e^3 \ln \Lambda / (4\pi \epsilon_0^2 m_e c^2)$ . The function  $Z$  characterizes the effect of pitch-angle scattering, which appears in the collision operator in the form of  $(1 + Z)$ . Equation (2) is an approximate fit [6] that combines the growth rate of REs at weak and strong electric field limits for different  $Z$ . Combining Eq. (2) with Eq. (1), the formation of runaway current plateau can be simulated. Once primary electrons are presented as  $I_{seed} \equiv I_{RE}(t = 0)$ , they are amplified until the ohmic current is totally dissipated and pre-disruption magnetic energy is converted into the steady-state RE current.

According to the R-P model [Eq. (2)], we can show that the avalanche theory needs a better estimation of the Coulomb logarithm than what is often assumed for high temperature plasmas. Taking the limit of  $E_{\parallel} \gg E_c$ , Eq. (2) reduces to a linear expression

$$\Gamma_{RP}^{(lin)} = \frac{E_{\parallel}/E_c}{a(Z)\tau \ln \Lambda}, \quad (3)$$

where  $a(Z) = \sqrt{3(Z+5)/\pi}$  is the function of  $Z$ . For  $Z = 1$ ,  $a(1) = 3(2/\pi)^{1/2}$ . From Eqs. (1) and (3), the amplification gain due to secondary generation  $I_{RE}(t = \tau_{CQ})/I_{RE}(t = 0) \simeq \exp(\Gamma_{RP}\tau_{CQ})$  is evaluated at the final point of CQ. By approximating the plasma inductance as  $L_p \simeq \mu_0 R_0$ , the electric field is estimated to be  $E_{\parallel} \simeq \mu_0 I_p / (2\pi\tau_{CQ})$ . Then we obtain the avalanche gain as a function of the plasma current:

$$\exp(\Gamma_{RP}\tau_{CQ}) = \left( \frac{2}{a(Z)I_A \ln \Lambda} I_p \right), \quad (4)$$

where  $I_A = 4\pi m_e c / (\mu_0 e) \simeq 17$  kA denotes the Alfvén current. For  $Z = 1$ , Eq. (4) reduces to  $\simeq \exp(2.7I_p[\text{MA}])$ , where the numerical factor 2.7 is obtained with  $\ln \Lambda_0 = 18$ . Equation (4) represents the capacity of runaway amplification during CQ. The argument  $\Gamma_{RP}\tau_{CQ}$  describes how much fraction of the pre-disruption magnetic flux  $\psi = L_p I_p \simeq \mu_0 R_0 I_p$  is converted into the flux carried by toroidally circulating relativistic electrons, where  $\psi_A \equiv \frac{1}{2}\mu_0 R_0 I_A \simeq 0.13$  V·s is the necessary flux for accelerating the electron ring up to the speed of light with the radius  $R_0$ . It is worth noting that a magnetic flux  $\psi_A$  is much smaller than the pre-disruption poloidal magnetic flux in large tokamaks,  $\psi_0 \simeq \mu_0 R_0 I_p \simeq 117$  V·s with  $R = 6.2$  m, being correlated to easier production of the RE current during CQ of high current tokamaks. The poloidal flux required for an  $e$ -fold [32] can be given as  $\psi_A a(Z) \ln \Lambda$ , which characterizes the efficiency of avalanche process, and indicates that the theory for avalanche needs to be accurate enough up to the order of  $O(1/\ln \Lambda)$ . Therefore, the treatment of the Coulomb logarithms becomes essential for the analysis. The fact that  $\Gamma_{RP}\tau_{CQ}$  is proportional to  $I_p$  shows that the disruption with higher plasma currents is susceptible to RE generation. In Ref. [33],  $I_{\text{seed}} = 4 \times 10^{-10}$  A has been estimated as a reference value for the seed current to obtain 7.5 MA in the case of ITER. In Ref. [31], the estimation of Eq. (4) has been refined without linearizing CQ, which is more optimistic but still  $I_{\text{seed}} = 10^{-3}$  A is estimated as the necessary seed current to obtain 1 MA RE current in Fig. 2 of Ref. [31]. This estimation is even much smaller than or comparable to seed currents produced by the tritium decay and the Compton scattering of gamma-rays in fusion devices [34].

## 2.2 Avalanche generation model near the critical threshold

While the approximate expression of electron-electron scattering cross section is employed in the R-P model, the avalanche growth rate taking into account a full expression has been developed [10, 16, 25]. In the latter case, the finite energy of primary electrons  $E_1 = (\gamma_1 - 1)m_e c^2$  is taken into account. In terms of the energy transfer variable  $\epsilon = (\gamma - 1)/(\gamma_1 - 1)$  with  $x \equiv 1/[\epsilon(1 - \epsilon)]$ , the Møller scattering cross section for electron-electron collisions is expressed as [35]

$$\frac{d\sigma_M(\epsilon; \gamma_1)}{d\epsilon} = 2\pi r_e^2 \frac{\gamma_1^2}{(\gamma_1 - 1)^2(\gamma_1 + 1)} \times \left[ x^2 - 3x + \left( \frac{\gamma_1 - 1}{\gamma_1} \right)^2 (1 + x) \right], \quad (5)$$

where  $\gamma_1$  and  $\gamma$  are the relativistic factor of incident and secondary electrons, respectively, and  $r_e = e^2/(4\pi\epsilon_0 m_e c^2)$  denotes the classical electron radius. The R-P model assumes the limit of  $\gamma_1 \rightarrow \infty$ , which yields  $d\sigma/d\gamma \simeq 2\pi r_e^2/(\gamma - 1)^2$ . Using the full expression of Eq. (5), the secondary generation rate is calculated from the probability for a primary electron to scatter thermal particles into the runaway region  $\gamma > \gamma_c$ , where the critical energy  $(\gamma_c - 1)m_e c^2$  characterizes the energy at which the acceleration by the electric field is balanced with the friction force exerted on the electrons. Hence the calculation of the scattering probability also needs to specify the energy of primary electrons. As postulated by the Fokker-Planck simulation [25], the distribution function of primary electrons can have a monoenergetic character, and the primary energy is approximated by the energy limit due to synchrotron and bremsstrahlung radiation [26]. Within this assumption, a general form of secondary electron generation rate is approximated with a given primary energy  $\gamma_1$  as

$$\Gamma_{\text{avl}}(\gamma_1) \equiv \frac{d \log n_{RE}}{dt} = n_e v_1 \int_{\epsilon_c}^{1/2} \frac{d\sigma_M(\epsilon; \gamma_1)}{d\epsilon} d\epsilon, \quad (6)$$

where  $v_1 = p_1/(m_e \gamma_1) \simeq c$  and  $\epsilon_c = (\gamma_c - 1)/(\gamma_1 - 1)$ . Note that the electron density  $n_e$  in Eq. (6) involves both free and bounded electrons  $n_e = n_{ef} + n_{eb}$  because both primary and critical energies are typically higher than the binding energy of electrons in impurity atoms. In Eq. (6), the upper bound of the integration is taken as 1/2 because a particle having higher energy after collision is regarded as a primary.

Under the assumption for deriving Eq. (6) the evaluation of avalanche growth rate reduces to the estimation of the energy of primary electrons  $\gamma_1$  and the critical energy transfer  $\epsilon_c = (\gamma_c - 1)/(\gamma_1 - 1)$ . When the pitch-angle scattering ( $Z = -1$ ) and the radiation is neglected, the Connor-Hastie limit [36] is applied. The critical energy and the momenta are evaluated as

$$\gamma_c = \sqrt{\frac{E/E_c}{(E/E_c) - 1}}, \quad (7)$$

$$q_c = \sqrt{\gamma_c^2 - 1} = \sqrt{\frac{1}{(E/E_c) - 1}}, \quad (8)$$

where  $q \equiv p/(m_e c)$  denotes the normalized relativistic momentum. The above estimation with  $Z = -1$  is modified by taking into account the pitch-angle scattering due to bulk ions ( $Z \simeq 1$ ) and impurities. The electron friction force is enhanced with bounded electrons [9], which makes  $\gamma_c$  higher and lowers probability for thermal electrons to be

scattered into the runaway region. In addition, impurities affect the estimation of the primary electron energy. The pitch-angle scattering due to the atomic nuclei enhances the synchrotron radiation loss, which modifies the flow pattern in the momentum space and affects the energy limit  $\gamma_1$  for primary electrons [26]. With high impurity content, the effects of bremsstrahlung radiation can also be significant [37] as a stopping mechanism for relativistic electrons.

Although Chiu, *et al.* [10] have shown that the introduction of finite energy of primary electrons does not affect the estimation of the avalanche growth rate so significantly when the electric field is strong,  $E_{\parallel} \gg E_c$ , Aleynikov and Breizman [25] have recently shown a qualitative change near the critical threshold  $E \simeq E_c$ . It is related to the upper bound of the integration of Eq. (6). According to the energy conservation, the energy of primary electrons after a collision is given as  $\gamma'_1 = \gamma_1 - \epsilon(\gamma_1 - 1)$ , for the multiplication, which should have the value higher than  $\gamma_c$ . It determines the condition for the multiplication such that  $\epsilon < \epsilon_a \equiv (\gamma_1 - \gamma_c)/(\gamma_1 - 1)$ . One can see that if  $\epsilon_a < 1/2$ , Eq. (6) gives a negative  $\Gamma_{\text{avl}} < 0$ . Consequently, the so-called sustainment field  $E_a$  is defined from the condition of  $\epsilon_a \simeq 1/2$  as the electric field for which the avalanche is marginal  $\Gamma_{\text{avl}} \simeq 0$ . Below this threshold,  $E_c < E_{\parallel} < E_a$ , the runaway current damps through the ‘inverse’ avalanche process. During the RE decaying process, the electric field is sustained to be slightly higher than the critical threshold [25]. As the consequence, combining Eq. (6) with Eq. (1), the simulation is allowed to evaluate the slow collisional damping of runaway current. This is an essential feature of the avalanche theory near the critical threshold, on the contrary to the conventional R-P model.

It must be noted that Eq. (6) cannot straightforwardly be applied to arbitrary electric fields. This is because the avalanche growth rate of Eq. (6) approximates the runaway condition one-dimensionally. By solving the binary collision problem of relativistic electrons, the pitch-angle distribution of secondary electrons is given as

$$\Pi(q_1, \xi_1, q, \xi) = \frac{1}{\pi \sqrt{|\xi_\beta^2 - (\xi - \xi_\alpha)^2|}}, \quad (9)$$

$$\xi_\alpha = \sqrt{\frac{\gamma_1 + 1}{\gamma_1 - 1} \frac{\gamma - 1}{\gamma + 1}} \xi_1, \quad (10)$$

$$\xi_\beta = \sqrt{\frac{2(\gamma_1 - \gamma)}{(\gamma_1 - 1)(\gamma + 1)}} (1 - \xi_1^2), \quad (11)$$

where  $\Pi(q_1, \xi_1, q, \xi)$  represents the probability such that a secondary electron with the momentum  $q$ , being scattered by primary one having the momentum and pitch  $(q_1, \xi_1)$ , will have a pitch in the range  $\xi + d\xi$  after single collision [38]. Taking the high velocity limits  $\gamma_1 \rightarrow \infty$  and  $\xi_1 \rightarrow 1$ , we obtain  $\Pi(q_1, \xi_1, q, \xi) \rightarrow \delta(\xi - \xi_\alpha)$  with  $\xi_\alpha \simeq \sqrt{\gamma - 1/\gamma + 1}$ , which implies that secondary electrons are scattered almost perpendicularly by close collisions. Such 2D features must be taken into account by the runaway

condition for secondary electrons, resulting in a modification of the avalanche growth rate by up to a factor of 2. To see this, we apply the momentum-dependent expression of the R-P model [6]

$$S(q, \xi) = \frac{n_{\text{RE}}}{4\pi\tau \ln \Lambda} \frac{1}{q^2} \frac{\partial}{\partial q} \left[ \frac{1}{1 - \sqrt{1 + q^2}} \right] \delta(\xi - \xi_\alpha). \quad (12)$$

With the assumption that a primary electron is highly relativistic  $\gamma_1 \gg 1$  at the strong electric field limit, Eq. (12) is integrated along the curve that represents the secondary electrons’ momenta in the 2D momentum space. Since the avalanche growth rate is defined as  $\Gamma_{\text{RP}} = n_{\text{RE}}^{-1} \int_{q_c}^{\infty} dq \int_{-1}^1 d\xi 2\pi q^2 S(q, \xi)$ , one obtains

$$\Gamma_{\text{RP}} = \frac{1}{2 \ln \Lambda \tau} \left[ \frac{1}{1 - \gamma} \right]_{\gamma_c}^{\infty} \approx \frac{eE_c}{2m_e c \ln \Lambda} \frac{1}{q_{\parallel c}}, \quad (13)$$

where in the last equality, we take into account that for secondary electrons, the parallel momentum satisfies the relation  $q_{\parallel} = \gamma - 1$  (see, Eq. (5) of Ref. [39]). The lower bound of integration of Eq. (13), the parallel critical momentum  $q_{\parallel c}$ , specifies the condition such that a particle starting from  $(q, q_{\parallel} = \sqrt{1 + q^2} - 1)$  as a secondary electron becomes runaway. The linear expression of the R-P model in Eq. (3) applies the runaway condition that  $q^2 > 2/(E/E_c - 1)$  [9], which yields  $\frac{1}{\gamma_c - 1} \simeq \frac{2}{q_c^2} = \frac{E}{E_c} - 1$  in Eq. (13). As the result, the avalanche growth rate of Eq. (7) of Ref. [6] for  $Z = -1$  is smaller by up to a factor 2 than those obtained by applying the Connor-Hastie critical momentum of Eq. (7) to Eq. (6). We emphasize that this contribution can never be dropped off for quantitatively reproducing the strong electric field limit. On the contrary, in the weak field limit, Parks, *et al.* [39] have shown that the secondary generation point and the critical one (determined by the balance between acceleration and friction) become arbitrary close in the momentum space. Therefore, the 1D treatments like Eq. (6) can still be applied.

### 3. Implementation of Impurity Models

In a post-disruption condition relevant to the RE generation, the electron temperature is typically around or less than 10 eV and a rich of partially stripped ions exist. In particular to the cases of massive gas injection, the impurity density on the order of  $10^{20} - 10^{21}/\text{m}^3$  is expected [2]. For taking into account the effect of such a high impurity content, the collision model for impure plasmas [24] is implemented in the INDEX code, where a charge-resolved expression of the Coulomb logarithm is considered. The plasma parameter during CQ is characterized by the power balance between ohmic heating and the radiative loss [23]

$$\eta J_{\text{Oh}}^2 \approx P_{\text{rad}} = n_{\text{ef}} \sum_s \sum_j n_s^{j+} L_{\text{rad},s}^{j+}(n_e, T_e), \quad (14)$$

where  $j_{\text{Oh}}$  is the pre-disruption ohmic current,  $n_{\text{ef}}$  is the free electron density, and  $n_s^{j+}$  is the impurity ion density. Equation (14) can be solved with given current density  $j_{\parallel}$ , the bulk ion density  $n_{\text{H}}$ , and electron temperature  $T_e$ , which determines the impurity density  $n_s^{j+}$  at the power balance, and the free and bounded electron density,  $n_{\text{ef}}$  and  $n_{\text{eb}}$ , as well as  $Z_{\text{eff}}$ . Equation (14) is solved numerically by iteration with coupling to the quasi-neutrality. The data for the radiation function  $L_{\text{rad},s}^{j+}(n_e, T_e)$  is here implemented using the OpenADAS database [40].

For impure plasmas, including the contribution of partially stripped ions, the friction force acting on test electrons can be written by

$$\mathbf{F}_e = -\frac{\alpha_e e^4 m_e \gamma (\gamma + 1)}{4\pi\epsilon_0^2 p^3} \mathbf{p}, \quad (15)$$

$$\mathbf{F}_i = -\frac{\alpha_e m_e Z_{\text{coll}} \gamma}{4\pi\epsilon_0^2 p^3} \mathbf{p}. \quad (16)$$

Here the functions  $\alpha_e$  and  $Z_{\text{coll}}$  are introduced to describe the friction and pitch-angle scattering due to partially stripped ions [19], which specify weak energy dependence through the Coulomb logarithm. For fully ionized plasmas,  $\alpha_e$  and  $Z_{\text{coll}}$  reduce to  $\alpha_e \rightarrow n_e \ln \Lambda$  and  $Z_{\text{coll}} \rightarrow Z_{\text{eff}} = \sum Z_i^2 n_i / n_e$ . We now define a charge-resolved expression of  $\alpha_e$  and  $Z_{\text{coll}}$  for arbitrary impurity species as follows:

$$\alpha_e = n_{\text{ef}} \ln \Lambda_{\text{ef}} + \sum_s \sum_j (Z_s^0 - Z_s^{j+}) n_s^{j+} \ln \Lambda_{\text{eb}}(s^{j+}), \quad (17)$$

$$Z_{\text{coll}} = \alpha_e^{-1} (n_{\text{H}} \ln \Lambda_{\text{eH}} + \sum_s \sum_j n_s^{j+} [(Z_s^{j+})^2 \ln \Lambda_{\text{eZ}}(s^{j+}) + (Z_s^0)^2 \ln \Lambda_{\text{eA}}(s^{j+})]). \quad (18)$$

In Eqs. (17) and (18), hydrogen is assumed to be fully ionized. The summation is taken over the species ( $s$ ) and the charge state ( $j+$ ), where  $n_{\text{ef}}$  is the free electron density,  $Z_s^0$  is the atomic charge,  $Z_s^{j+}$  is the unshielded ion charge, and  $n_s^{j+}$  is the ion (or atom) density.

A possible approximation to describe the Coulomb logarithms in Eqs. (17) and (18) has been presented by Mosher [24], while as was suggested in the footnote of [24], his estimate can be refined to include the quantum mechanical correction as well as the effect of plasma wave excitation. Such a modification can be found in the literatures. For collisions with free electrons,  $\ln \Lambda_{\text{ef}}$ , the formula including the quantum mechanical correction as well as higher-order effects can be found in Ref. [41], where the Coulomb logarithm for collisions between free electrons  $\ln \Lambda_{\text{ef}}$  is given as

$$\ln \Lambda_{\text{ef}}^{\text{ef}} = \frac{1}{2} \left[ \ln \left( \frac{m^2 c^2 (\gamma - 1) \lambda_{\text{D}}^2}{2 \hbar^2} \right) + 1 + \frac{1}{8} \left( \frac{\gamma - 1}{\gamma} \right)^2 - \frac{2\gamma - 1}{\gamma^2} \ln 2 \right]. \quad (19)$$

This expression involves a quantum mechanical correction that for the relevant parameter range, the classical Landau parameter is smaller than the de Broglie wavelength  $\lambda_{\text{db}}$ , where  $\lambda_{\text{db}} = \hbar / [m_e c \sqrt{(\gamma - 1)}]$  in the center-of-mass system. Equation (19) is further modified by including the energy loss due to the excitation of plasma wave (see Eq. (10) of Ref. [41]),

$$\ln \Lambda_{\text{ef}} = \frac{1}{2} \left[ \ln \left[ \left( \frac{\mathcal{E}}{\hbar \omega_p} \right)^2 \frac{\gamma + 1}{2\gamma^2} \right] + 1 + \frac{1}{8} \left( \frac{\gamma - 1}{\gamma} \right)^2 - \frac{2\gamma - 1}{\gamma^2} \ln 2 \right], \quad (20)$$

where  $\mathcal{E}$  is the electron kinetic energy, and  $\omega_p$  is the plasma frequency. Note that even though the maximum impact parameter is determined by the Debye length, the contribution of plasma wave excitation cancels the dependence on the background temperature. In Fig. 1 (a),  $\ln \Lambda_{\text{ef}}$  is compared with and without the correction due to plasma wave excitation as well as against the classical expression  $\ln \Lambda_{\text{ef}} = \ln[(\gamma - 1)(\gamma + 1)^{1/2} \lambda_{\text{D}} / (2\gamma r_e)]$ . We find that the full

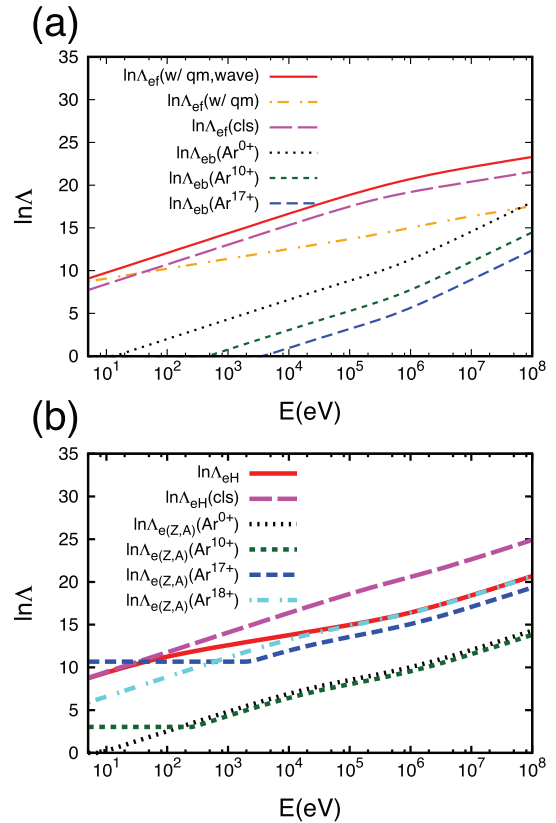


Fig. 1 Charge-resolved Coulomb logarithms calculated for (a) electron-electron and (b) electron-ion collisions using Eqs. (20)-(24) for  $n_{\text{H}} = 10^{20} \text{ m}^{-3}$ ,  $T_e = 5 \text{ eV}$ ,  $n_{\text{Ar}} = 1.3 \times 10^{19} \text{ m}^{-3}$ ,  $n_{\text{ef}} = 1.3 \times 10^{20} \text{ m}^{-3}$ ,  $n_{\text{eb}} = 2.0 \times 10^{20} \text{ m}^{-3}$ , and  $Z_{\text{eff}} = 1.4$ . Dash-dotted curve in the top figure represents  $\ln \Lambda_{\text{ef}}$  without the wave excitation effect and long-dashed curves in both figures represent the classical estimation with  $b_{\text{min}} = b_{\text{L}}$  for  $\ln \Lambda_{\text{ef}}$  and  $\ln \Lambda_{\text{eH}}$ .

expression indicated by the red solid curve [Eq. (20)] and the classical one (the magenta long-dashed one) give similar results. However, this is an accidental agreement, because while the quantum mechanical correction (indicated by the orange dot-dashed curve) weakens the friction, the energy loss due to the plasma excitation recovers the friction force up to the level slightly stronger than the classical estimation.

For electron-ion collisions, the classical expression  $\ln \Lambda_{eH} = \ln[(\gamma^2 - 1)\lambda_D/(\gamma r_e)]$  is modified in the form of  $\ln \Lambda = \frac{1}{2} \ln[1 + (b_{\max}^2/b_{\min}^2)]$ . It requires *ad hoc* cut-off  $b_{\max}$ , which is normally set to be the Debye length  $\lambda_D$ . For a dense system we also take into account the ion sphere radius  $a_i = (3/4\pi n_i)^{1/3}$ , where  $n_i$  is the ion density. To reproduce  $\ln \Lambda$  in dilute plasmas, we can employ  $b_{\max} = (\lambda_D^2 + a_i^2)^{1/2}$  [42]. The lower cutoff is estimated here by  $b_{\min} = [b_L + (\lambda_{db}/2)]^{1/2}$ , where  $b_L = Zr_e/(\gamma\beta^2)$  is the Landau parameter and  $\lambda_{db} = \hbar/(\gamma m_e c\beta)$  is the de Broglie wavelength with  $\beta = v/c$ . The classical result is reproduced by simply setting  $b_{\min} = b_L$ . In Fig. 1 (b),  $\ln \Lambda_{eH}$  is compared with and without the quantum mechanical correction by the solid and long-dashed curves, where we see 15 - 20 % reduction of  $\ln \Lambda_{eH}$  at the MeV-order range of incident electron energy. For a wide range of the parameter, the quantum mechanical correction can be significant, where  $b_L/b_{db} = Z/\beta\alpha$  is less than unity, other than the cases with low electron kinetic energy  $\beta \ll 1$  and for collisions with high  $Z$  ions (where  $\alpha = e^2/(2\epsilon_0\hbar c) = 1/137$  denotes the fine structure constant).

Collisions with impurity ions (or atoms) of the species  $s$  with the charge  $j+$  consist of three parts: (i) friction due to bounded electrons,  $\ln \Lambda_{eb}(s^{j+})$ , (ii) friction due to unshielded ion charge  $Z_s^{j+}$ ,  $\ln \Lambda_{eZ}(s^{j+})$ , and (iii) elastic scattering due to atomic nuclei with charge  $Z_s^0 \ln \Lambda_{eA}(s^{j+})$ . We employ the following model to evaluate the contribution of (ii) and (iii):

$$\ln \Lambda_{eZ} = \ln\left(\frac{\lambda_D}{\lambda_A}\right), \quad (21)$$

$$\ln \Lambda_{eA} = \ln\left(\frac{\lambda_A}{b_{\min}}\right), \quad (22)$$

where  $b_{\min}$  is defined in a same way with the hydrogen, and  $\lambda_A$  is the measure of the size of electron orbital radius. We simplify the treatment of  $\lambda_A$  in terms of the ionization energy of most loosely bounded electron, where  $\lambda_A = (mc^2/I_s^{(j+1)+})Z_s^0 r_e$ , where  $I_s^{(j+1)+}$  is the ionization energy for the reaction from  $j$ -th stage to  $(j+1)$ -th one. This simple model is useful to estimate the charge stage dependence of Eqs. (21) and (22) using the existing database of the ionization potential. We employ the ionization energy data available in the OpenADAS database [40] except that Ref. [43] is used for Tungsten ions in our numerical code. In Fig. 1 (b), Eqs. (21) and (22) are evaluated as  $\ln \Lambda_{e(Z,A)} = [(Z_s^{j+})^2 \ln \Lambda_{eZ}(s^{j+}) + (Z_s^0)^2 \ln \Lambda_{eA}(s^{j+})]/(Z_s^0)^2$  for argons with four different charge states,  $\text{Ar}^{0+}$  (black),  $\text{Ar}^{10+}$  (green),  $\text{Ar}^{17+}$  (blue), and  $\text{Ar}^{18+}$  (cyan). When

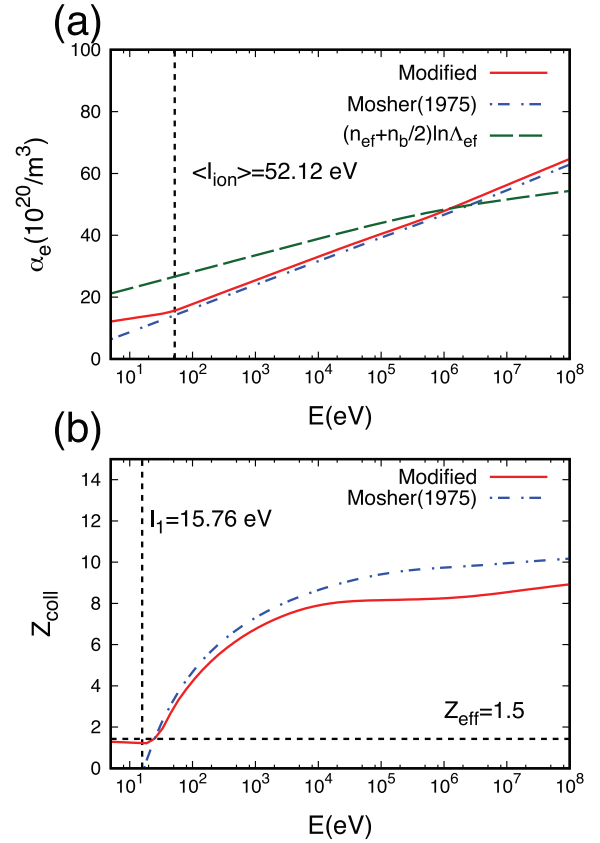


Fig. 2 The dependence of electron and ion friction functions  $\alpha_e$  and  $Z_{coll}$  on the incident electron energy. Blue dot-dashed curves are calculated with the expressions of [23] based on Moshier [24] which assumes  $b_{\min} = b_L$  and single ions with the averaged charge for each atomic species. Long-dashed curve in the top figure indicates a simple estimate of the electron friction function,  $(n_{ef} + n_b/2) \ln \Lambda_{ef}$  [9].

focusing on the energy dependence  $\ln \Lambda_{e(Z,A)}$  for  $\text{Ar}^{10+}$  and  $\text{Ar}^{17+}$ , we see that at  $E > I_s^{(j+1)+}$  ( $E$ : the energy of the elastic scattering due to atomic nuclei, whereas at  $E < I_s^{(j+1)+}$ , i.e., if the energy of incident electrons is lower than the binding energy of orbital electrons, electrons interact with partially stripped impurity interacts only through the ion charge  $Z_s^{j+}$ , unshielded by the orbital electrons. While  $\ln \Lambda_{eZ}$  vanishes for neutrals  $\text{Ar}^{0+}$ , for fully stripped ions  $\text{Ar}^{18+}$ ,  $\ln \Lambda_{e(Z,A)}$  reduces to the same treatments for hydrogen as  $\ln(\lambda_D/b_{\min})$ . The remaining contribution is collisions with bounded electrons (i), which is taken into account by the modified Bethe-Bloch formula for electron collisions [44]

$$\ln \Lambda_{eb}(s^{j+}) = \ln\left[\frac{(\gamma - 1)(\gamma + 1)^{1/2}}{\sqrt{2} I_s^{(j+1)+}/mc^2} + \frac{F(\gamma)}{2}\right], \quad (23)$$

where higher-order correction  $F(\gamma)$  is given by

$$\frac{F(\gamma)}{2} = -\left(\frac{2}{\gamma} - \frac{1}{\gamma^2}\right) \frac{\ln 2}{2} + \frac{1}{2\gamma^2} + \frac{(\gamma - 1)^2}{16\gamma^2}. \quad (24)$$

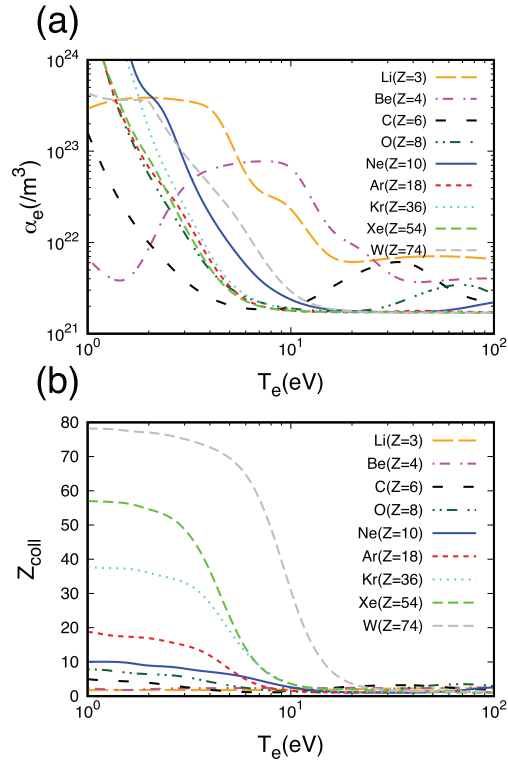


Fig. 3 Examples of the electron and ion friction functions  $\alpha_e$  and  $Z_{\text{coll}}$  for 1 MeV test electrons with different impurity species, where the background parameters are determined at the power balance described by Eq. (14) with the electron temperature  $T_e$  given on the  $x$ -axis.

In Fig. 1 (a), the contribution of bounded electrons is illustrated for  $\text{Ar}^{0+}$  (black),  $\text{Ar}^{10+}$  (green), and  $\text{Ar}^{17+}$  (blue), approximately being about a half of the free electron part of the Coulomb logarithm indicated by the red solid curve.

Figure 2 shows the electron and ion friction functions,  $\alpha_e$  and  $Z_{\text{coll}}$ , in Eqs. (17) and (18) for argons using our collection of the Coulomb logarithm [Eqs. (20)-(24)]. The results are compared with Fig. 1 of Ref. [23] based on Mosher [24], and with a simple estimate of the electron friction function such that  $\alpha_e \approx (n_{\text{ef}} + n_{\text{eb}}/2) \ln \Lambda_{\text{ef}}$  [9]. Because of the agreement of  $\ln \Lambda_{\text{ef}}$  between the modified and classical models, Fig. 2 (a) shows that  $\alpha_e$  agrees well with the previous work. We also see that the simple estimate  $(n_{\text{ef}} + n_{\text{eb}}/2) \ln \Lambda_{\text{ef}}$  works well at MeV order but overestimates the friction function  $\alpha_e$  at sub-relativistic energy. In Fig. 2 (b), we find a decrease of  $Z_{\text{coll}}$  up to 15 - 20% from the classical result at MeV-order range, which is due to the quantum mechanical correction to  $\ln \Lambda_{\text{eA}}$  (where the hydrogen contribution to  $Z_{\text{coll}}$  is small). We also see that  $Z_{\text{coll}}$  reduces to  $Z_{\text{eff}}$  when the incident energy drops below minimum ionization energy  $I_1$ , indicating that a charge-resolved model is working well. (Also, we see that  $\alpha_e$  is modified slightly in Fig. 2 (a) roughly speaking, at the incident energy below the average ionization potential  $\langle I \rangle$  for all charge states.) Figure 3 illustrates the electron and ion

friction functions,  $\alpha_e$  and  $Z_{\text{coll}}$ , for 1 MeV incident electrons, with different background temperature and impurity species. We observe that non-monotonic variation of the friction function  $\alpha_e$  depending on the impurity species, and the enhancement of  $Z_{\text{coll}}$  for high  $Z$  materials at the lower temperature. These features of  $\alpha_e$  and  $Z_{\text{coll}}$  significantly affect the parametric dependence of the runaway generation rate — mainly through the modification to the critical electric field required for runaways, and is essentially important for runaway electron mitigation.

## 4. Energy Limit, Critical Energy, and Avalanche Growth Rate

This section is devoted to the estimation of the critical energy and the energy limit, which are necessary for calculating the avalanche growth rate based on the near-critical threshold theory. In the INDEX code, two approaches have been implemented with the impurity collision model of Sec. 3. One employs analytic solutions of the Fokker-Planck equation, introduced by Aleynikov and Breizman [25] (which we call ‘A-B’ model). The other solves a trajectory of test particles in the momentum space [26] (which we call ‘mean particle (MP)’ model here). Below we briefly reproduce these two models following Ref. [25, 26] but we employ identical synchrotron and bremsstrahlung terms. In that case, a difference in these two models becomes whether the second-order collisional diffusion term is truncated or not. After that, these models are applied to the calculation of the avalanche growth rate, and the electric field dependence is compared against the adjoint Fokker-Planck code [29, 30].

### 4.1 Aleynikov-Breizman (A-B) model

Consider a relativistic kinetic equation

$$\tau_0 \frac{\partial f}{\partial t} + \hat{E} \mathbf{b} \cdot \nabla_{\mathbf{q}} f = C(f) + C_s(f) + C_B(f), \quad (25)$$

where  $\mathbf{q} = \mathbf{p}/(m_e c)$  represents the normalized relativistic momenta,  $f$  is the distribution function,  $C(f)$  is the collision term,  $C_s(f)$  is the synchrotron radiation loss, and  $C_B(f)$  represents bremsstrahlung radiation. The collision time  $\tau_0 = 4\pi\epsilon_0^2 m_e^2 c^3 / (n_e e^4 \ln \Lambda_0)$  is used as a normalization constant with the free electron density  $n_e = n_{\text{ef}}$  and a constant Coulomb logarithm  $\ln \Lambda_0 = 18$ . The normalized electric field is defined as  $\hat{E} = E_{\parallel}/E_{c0}$ , where  $E_{c0} = m_e c / e \tau_0 = n_{\text{ef}} e^3 \ln \Lambda_0 / (4\pi\epsilon_0 m_e c^2)$ . In this paper, the reference electric field  $E_{c0}$  is distinguished from  $E_c^*$  that is defined later to indicate the effect of bounded electrons and radiations. If one employs the momentum-space coordinate  $(q, \xi = q_{\parallel}/q)$ , where  $\parallel$  represents the direction along the magnetic field, each term of the Fokker-Planck equation is written as follows. The acceleration and collision terms are given by

$$\mathbf{b} \cdot \nabla_{\mathbf{q}} f = \xi \frac{\partial f}{\partial q} + \frac{1 - \xi^2}{q} \frac{\partial f}{\partial \xi}, \quad (26)$$

$$C(f) = \frac{1}{q^2} \frac{\partial}{\partial q} [A(q)(1+q^2)f] + \frac{A(q)(1+Z)}{2} \frac{\sqrt{1+q^2}}{q^3} \frac{\partial}{\partial \xi} (1-\xi^2) \frac{\partial f}{\partial \xi}, \quad (27)$$

where  $A(q) = \alpha_e/(n_{ef} \ln \Lambda_0)$  and  $Z(q) = Z_{\text{coll}}$  quantify the effects of impurity collisions. Note that the weak energy dependence of these terms through  $\ln \Lambda$  is treated as constant when manipulating Eq. (27). The synchrotron and bremsstrahlung reaction force is described in the following form:

$$C_s(f) = \frac{1}{q^2} \frac{\partial}{\partial q} (q^2 F_{\text{gy}} \gamma q (1-\xi^2) f) - \frac{\partial}{\partial \xi} \left( F_{\text{gy}} \frac{\xi(1-\xi^2)}{\gamma} f \right), \quad (28)$$

$$C_B(f) = \frac{1}{q^2} \frac{\partial}{\partial q} \left( q^2 F_{\text{br}} \alpha_Z \gamma \left( \ln 2\gamma - \frac{1}{3} \right) f \right), \quad (29)$$

where  $F_{\text{gy}} \equiv \tau_0/\tau_s$  represents the ratio of collision time  $\tau_0$  to the radiation time  $\tau_s = 6\pi\epsilon_0(m_e c)^3/(e^4 B^2)$ . The expression for bremsstrahlung follows a high  $\gamma$  limit in a similar way to Ref. [45] with  $\alpha_Z = (n_{ef} + n_{eb})(1 + Z_{A,\text{eff}})/n_{ef}$  and  $F_{\text{br}} = 1/(137\pi \ln \Lambda_0)$ . The effective  $Z$  for bremsstrahlung is evaluated with respect to the atomic charge as  $Z_{A,\text{eff}} = \sum_s [n_H + (Z_s^0)^2 n_s] / \sum_s (n_H + Z_s^0 n_s)$ , where the summation is taken over the impurity species and  $n_s$  is the atomic density for  $s$ -th species. In general, no simple expression for the bremsstrahlung cross section of electron-electron collision is available for arbitrary energy and  $Z$  [46] so that in Eq. (29) the expression for  $Z = 1$  is simply assumed, and the electron contribution becomes smaller than ion ones by up to the factor of  $1/Z_{A,\text{eff}}$ .

For the runaway study, although the mean force operator of bremsstrahlung like Eq. (29) has been used in both test-particle [45] and Fokker-Planck simulations [47], the treatment of bremsstrahlung as a continuous slowing down of the electrons loses its discrete picture when the emitted photons can have energies of the same order as the incident electrons. Recently, Embréus, *et al.* [48] have analyzed the bremsstrahlung emission of runaway electrons as binary interactions using the Boltzmann-type kinetic operator. Although such a kinetic treatment is beyond the scope of this work, the comparison of the Boltzmann and mean force operators has been illustrated in Figs. 1-2 of Ref. [48], showing that the maximum energy limit is less sharp in the Boltzmann case and the electron distribution function exhibits a broader spectrum in both energy and angular directions. Figure 3 of Ref. [48] has shown the maximum reachable energy is about twice the energy obtained using the mean force operator.

Equation (25) is rewritten in the form that can directly be compared to Ref. [25]. Defining  $\mathcal{F} \equiv q^2 f$ , Eq. (25) in the coordinate system  $(q, \theta)$ , where  $\theta \equiv \text{acos}(\xi)$ , one obtains

$$\begin{aligned} & \tau_0 \frac{\partial \mathcal{F}}{\partial t} + \frac{\partial}{\partial q} \left\{ \hat{E} \cos \theta - \left[ A + \frac{A}{q^2} + F_{\text{br}} \alpha_Z \gamma \right. \right. \\ & \times \left. \left. \left( \ln 2\gamma - \frac{1}{3} \right) \right] - F_{\text{gy}} q \sqrt{1+q^2} \sin^2 \theta \right\} \mathcal{F} \\ & = \frac{1}{\sin \theta} \frac{\partial}{\partial \theta} \sin \theta \left[ \hat{E} \frac{\sin \theta}{q} \mathcal{F} + A \frac{(1+Z)}{2} \frac{\sqrt{1+q^2}}{q^3} \frac{\partial \mathcal{F}}{\partial \theta} \right. \\ & \quad \left. + F_{\text{gy}} \frac{\cos \theta \sin \theta}{\gamma} \mathcal{F} \right]. \end{aligned} \quad (30)$$

Applying the assumption such that the equilibration in the pitch-angle direction is much faster than the energy drag and that the radiation loss is weaker than the collisional loss, a solution to the lowest-order equation

$$\frac{1}{\sin \theta} \frac{\partial \mathcal{F}}{\partial \theta} + \mathcal{K} \mathcal{F} = 0, \quad (31)$$

$$\mathcal{K}(q) = \frac{2\hat{E}}{Z+1} \frac{q^2}{A \sqrt{1+q^2}}, \quad (32)$$

is found to be [25]

$$\mathcal{F} = G(t; q) \frac{\mathcal{K}}{2 \sinh \mathcal{K}} \exp[\mathcal{K} \cos \theta]. \quad (33)$$

Inserting this solution to the left-hand side of Eq. (30) and integrated over the pitch angle as  $\int_0^\pi d\theta \sin \theta$ , one obtains

$$\tau_0 \frac{\partial G}{\partial t} + \frac{\partial}{\partial q} U(q) G(t; q) = 0, \quad (34)$$

where the flow function  $U(q)$  is given by

$$\begin{aligned} U(q) = & - \left( \frac{1}{\mathcal{K}} - \frac{1}{\tanh \mathcal{K}} \right) \hat{E} \\ & - \left[ A + \frac{A}{q^2} + F_{\text{br}} \alpha_Z \gamma \left( \ln 2\gamma - \frac{1}{3} \right) \right] \\ & + \frac{Z+1}{\hat{E}} \frac{A(1+q^2)}{q} F_{\text{gy}} \left( \frac{1}{\mathcal{K}} - \frac{1}{\tanh \mathcal{K}} \right). \end{aligned} \quad (35)$$

In Eq. (35), being different from Eq. (7) of Ref. [25], the bremsstrahlung term is included here. The flow function  $U(q)$  calculated by the A-B model is illustrated in Fig. 4 (a) with the red curves, where the nonlinear equation  $U(q) = 0$  with a maximum flow velocity  $\gamma(U_{\text{max}})$  have two roots representing the energy limit  $\gamma_1$  (stable) and the critical energy  $\gamma_c$  (unstable). The sensitivity of the results to the bremsstrahlung radiation is also illustrated by the dashed curve. Once we obtain the equilibrium points  $\gamma_1$  and  $\gamma_c$ , the corresponding average of the pitch is calculated as

$$\langle \cos \theta \rangle = \frac{(\mathcal{K} - 1)e^{\mathcal{K}} + (\mathcal{K} + 1)e^{-\mathcal{K}}}{\mathcal{K}(e^{\mathcal{K}} - e^{-\mathcal{K}})}, \quad (36)$$

which can be used as an estimate of the pitch-angle of primary electrons when it is applied to the energy limit,

$$U(q_1 \equiv \sqrt{\gamma_1^2 - 1}) = 0.$$

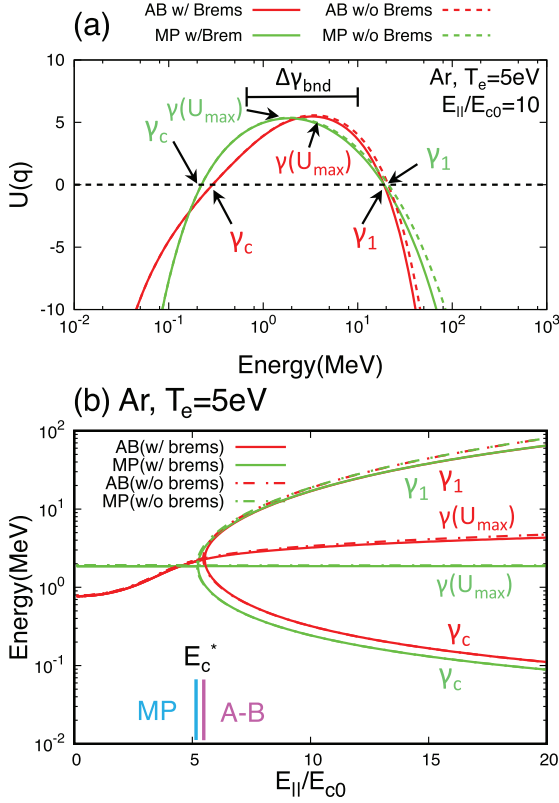


Fig. 4 (a) Flow function  $U(q)$  calculated by the A-B and MP models as functions of the energy with and without bremsstrahlung radiation. (b) The 2D map of the characteristic roots  $\gamma_c$ ,  $\gamma(U_{max})$ , and  $\gamma_1$  as function of the electric field for  $T_e = 5$  eV with argon impurity. The magenta and cyan bars indicate the critical electric field  $E_c^*$  including the effects of synchrotron and bremsstrahlung radiation as well as that of the friction force due to bounded electrons.

## 4.2 Mean particle (MP) model

In the previous work, the mean particle (MP) equation has been employed to obtain an intuitive picture of the runaway trajectory in the momentum space [49]. It is also used to evaluate the effect of synchrotron [26] and bremsstrahlung radiation losses [45] as well as the avalanche growth rate [39]. By noting that the test particle equation  $\frac{dq}{dt} = \mathbf{F}$  corresponds to the partial differential equation in the conservative form  $\frac{\partial f}{\partial t} = -\frac{\partial}{\partial \mathbf{p}} \cdot \mathbf{F} = -\frac{1}{p^2} \frac{\partial}{\partial p} (p^2 \hat{\mathbf{p}} \cdot \mathbf{F}) - \frac{\partial}{\partial \xi} (\xi \cdot \mathbf{F})$ , we obtain the ordinary differential equation from Eq. (25), by truncating the second-order diffusion term. Following Ref. [26], we write the mean particle equation in the  $(q_{||}, q)$  coordinate as

$$\tau_0 \frac{dq_{||}}{dt} = \hat{E} - A \frac{\gamma(\alpha + \gamma)}{q^2} \frac{q_{||}}{q} - F_{gy} \frac{q^2 q_{||} (1 - \xi^2)}{\gamma} - F_{br} \alpha Z \gamma \left( \ln 2\gamma - \frac{1}{3} \right) \frac{q_{||}}{q}, \quad (37)$$

$$\tau_0 \frac{dq}{dt} = \hat{E} \frac{q_{||}}{q} - A \frac{\gamma^2}{q^2} - F_{gy} \gamma q (1 - \xi^2) - F_{br} \alpha Z \gamma \left( \ln 2\gamma - \frac{1}{3} \right). \quad (38)$$

Note that although the original work [26] employs a different approximation to the radiation reaction force [50], we apply the same one with Eq. (25) and those used in Refs. [51, 52]. By solving  $dq/dt = 0$  to get stagnation points ( $q_s = \sqrt{\gamma_s^2 - 1}$ ,  $\xi_s = \cos \theta_s$ ) of the momentum-space flow, we obtain  $\hat{E} = V(\gamma_s, \theta_s)$ , where

$$V(\gamma_s, \theta_s) \equiv \frac{\gamma_s^2}{(\gamma_s^2 - 1) \cos \theta_s} \left[ A + \frac{(\gamma_s^2 - 1)^{3/2}}{\gamma_s} \times F_{gy} \sin^2 \theta_s + \frac{(\gamma_s^2 - 1)}{\gamma_s} F_{br} \alpha Z \left( \ln 2\gamma_s - \frac{1}{3} \right) \right]. \quad (39)$$

Next we evaluate the cosine of pitch angle  $\cos \theta_s$  as a function of  $\gamma_s$ . From the relation  $dq_{\perp}/dt = 0$ , we obtain a quadratic equation for  $\sin^2 \theta_s$  as

$$\sin^4 \theta_s + \sin^2 \theta_s \frac{\gamma_s^2 (\alpha + \gamma_s)}{F_{gy} (\gamma_s^2 - 1)^{5/2}} \times \left[ A + \frac{(\gamma_s^2 - 1)^{3/2}}{\gamma_s^2 (\alpha + \gamma_s)} F_{gybr} \right] - \frac{A \gamma_s^2 \alpha}{F_{gy} (\gamma_s^2 - 1)^{5/2}} = 0, \quad (40)$$

where

$$F_{gybr} = F_{gy} + \frac{\gamma_s^2}{(\gamma_s^2 - 1)^{1/2}} F_{br} \alpha Z \left( \ln 2\gamma_s - \frac{1}{3} \right).$$

The solution less than unity from Eq. (40) is chosen and we finally obtain

$$\cos^2 \theta_s = 1 + \frac{F_{gybr}}{2F_{gy}(\gamma_s^2 - 1)} + \frac{\gamma_s^2 (\alpha + \gamma_s)}{2F_{gy}(\gamma_s^2 - 1)^{5/2}} \times \left\{ A - \left[ \left( A + \frac{(\gamma_s^2 - 1)^{3/2}}{\gamma_s^2 (\alpha + \gamma_s)} F_{gybr} \right)^2 + \frac{4A\alpha F_{gy} (\gamma_s^2 - 1)^{5/2}}{\gamma_s^2 (\alpha + \gamma_s)^2} \right]^{1/2} \right\}. \quad (41)$$

Equations (39) and (41) specify the flow function  $U^{MP}(q) \equiv \hat{E} - V$ , which can directly be compared with the A-B model. Two roots for  $U^{MP}(q) = 0$  are compared with those obtained by Eq. (35) in Fig. 4(a). Because of the use of identical synchrotron and bremsstrahlung radiation terms, a close agreement of the energy limit  $\gamma_1$  is obtained. On the contrary, we see that  $\gamma_c$  obtained by the MP model is lower than those obtained by the A-B model. Such a lower estimation of  $\gamma_c$  by the MP model is attributed to the truncation of second-order diffusion term. In Fig. 4(b) the characteristic roots calculated by the A-B and MP models are illustrated as a function of the electric fields. It shows that the MP model tends to underestimate  $\gamma_c$  over the full range of electric fields exceeding the critical threshold  $E_c^*$ . In Fig. 4(b), magenta and cyan bars indicate the values of the resultant critical electric field  $E_c^*$ ,

including the effects of synchrotron and bremsstrahlung radiation as well as that of the friction force due to bounded electrons. They are defined as the electric field at which the two roots  $\gamma_c$  and  $\gamma_1$  in the momentum-space flow merge. A main effect of bremsstrahlung is to decrease the energy limit  $\gamma_1$ , which plays a minor role in the critical energy  $\gamma_c$ .

### 4.3 Adjoint Fokker-Planck code and avalanche growth rate

The avalanche growth rate based on the near-critical threshold theory is calculated by inserting the critical energy and the energy limit obtained by the A-B or MP models into Eq. (6). However, as was discussed in Sec. 2.2, the resultant growth rate is not applied in a unified way to the strong electric field limit. For obtaining the expression that can be applied to a wide range of the electric fields, we begin with the comparison of the near-critical threshold theory and the R-P model to the third method — based on the adjoint Fokker-Planck equation [29]. Details of the adjoint Fokker-Planck method have been described by Liu and the co-authors [29, 30]. Here the Fokker-Planck code to solve the adjoint equations has been implemented with the finite difference method, as what has been reviewed in Ref. [28], and the friction and radiation coefficients have been implemented with the same way with what is described in Sec. 4.1. The numerical solution provides the runaway probability  $0 \leq \mathcal{P}(\gamma, \theta) \leq 1$  with the boundary condition  $\mathcal{P}(\gamma_{\text{bnd}}, \theta) = 1$  and  $\mathcal{P}(0, \theta) = 0$ , where  $\gamma_{\text{bnd}}$  denotes the Lorentz factor at the computational boundary and  $\theta = \text{acos}(\xi)$  denotes the pitch angle. The calculated runaway probability is combined with the Møller scattering cross section of Eq. (5), and the avalanche growth rate is calculated as

$$\begin{aligned} \Gamma_{\text{avl}}(\gamma_1, \theta_1) = n_e c \int_0^{1/2} d\epsilon \int_0^\pi d\theta \frac{d\sigma_M(\epsilon; \gamma_1)}{d\epsilon} \\ \times \{ \delta(\theta - \theta') \delta(\gamma - \gamma') \mathcal{P}(\gamma, \theta) \\ - \delta(\theta - \theta'_1) \delta(\gamma - \gamma'_1) (1 - \mathcal{P}(\gamma, \theta)) \}, \end{aligned} \quad (42)$$

where the second term represents the scattering of primary electrons into lower energy, and  $(\gamma'_1, \theta'_1)$  and  $(\gamma', \theta')$  denote the position of primary and secondary electrons in the momentum space after single collision. Near the critical thresholds, the second term of Eq. (42) dominates over the integral, which reproduces the negative growth (damping) rate of the near-critical threshold theory. For calculating  $\mathcal{P}(\gamma, \theta)$ , the momentum space boundary  $\gamma_{\text{bnd}}$  must be selected appropriately in the runaway region. In the following, we will check the sensitivity of our results to the momentum space boundary where the Lorentz factor at the boundary  $\gamma_{\text{bnd}}$  is varied from  $[\gamma_c + \gamma(U_{\text{max}})]/2$  to  $[\gamma(U_{\text{max}}) + \gamma_1]/2$ , the corresponding range  $\Delta\gamma_{\text{bnd}}$  being displayed in Fig. 4 (a). Such sensitivities to  $\gamma_{\text{bnd}}$  are physically connected to those to the shape of the runaway electron distribution function that is sustained by the avalanche. To eliminate such a subtlety in calculating the growth

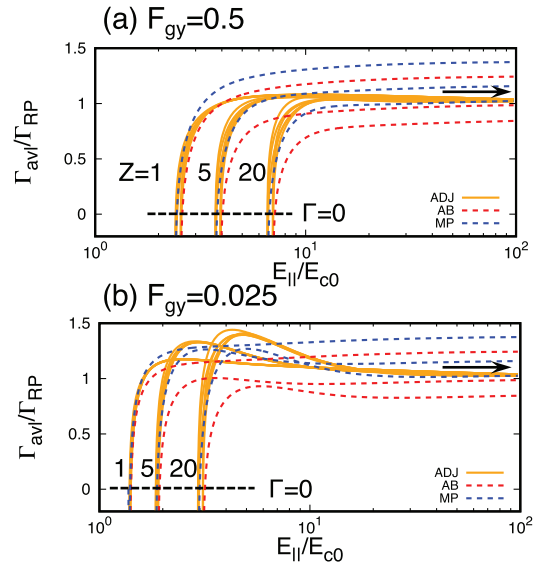


Fig. 5 The avalanche growth rates normalized by the R-P model [Eq. (2)]. Red and blue dashed curves correspond to Eq. (6) evaluated using the A-B and MP models, respectively. The solid curves are drawn for the adjoint Fokker-Planck method [Eq. (42)], where six different values of the momentum-space boundary  $\gamma_{\text{bnd}}$  in the range from  $[\gamma_c + \gamma(U_{\text{max}})]/2$  to  $[\gamma(U_{\text{max}}) + \gamma_1]/2$  are applied.

rate, a more sophisticated method to obtain the distribution function as an eigenvector has been proposed recently in Eqs. (28) and (29) of Ref. [30].

In Fig. 5, we compare the avalanche growth rate calculated by the A-B and MP models with Eq. (6) to the adjoint Fokker-Planck method. For this comparison, the R-P model is used as a reference so that the calculated growth rate is normalized by Eq. (2) at the same electric field. For the clarity of the benchmark, the friction coefficients  $A(q) = \alpha_c(q)/(n_{ef} \ln \Lambda_0)$  and  $Z(q)$  as well as the Coulomb logarithm are set by  $A(q) = 1$  and  $Z(q) = \text{const.}$  with  $\ln \Lambda_0 = 18$ . In Fig. 5, we first look at the strong electric field limit  $E_{||}/E_{c0} \approx 10^2$  (indicated by the black arrows) and find that the adjoint Fokker-Planck code well reproduce the R-P limit for different  $Z$  as  $\Gamma_{\text{avl}}/\Gamma_{\text{RP}} \approx 1$ . This follows the discussion in Sec. 2.2, and neither A-B nor MP models can reproduce this limit. Secondly, we also see that the sustainment field  $E_a$ , i.e., the electric field at  $\Gamma_{\text{avl}} \approx 0$  (indicated by the black dashed segments) agrees well between the different models, within the sensitivity of the adjoint Fokker-Planck method to the selection of momentum space boundary. We mention that to get better evaluations of the sustainment fields, the approach should be refined to take into account the shape of the runaway distribution function, which is beyond the scope of the present analysis.

Next a focus is placed on the avalanche growth rate in the intermediate electric fields between the sustainment field and the strong electric field. In the previous work [25], it was emphasized that the A-B model asymptotes to the weak field limit of the R-P model, where we

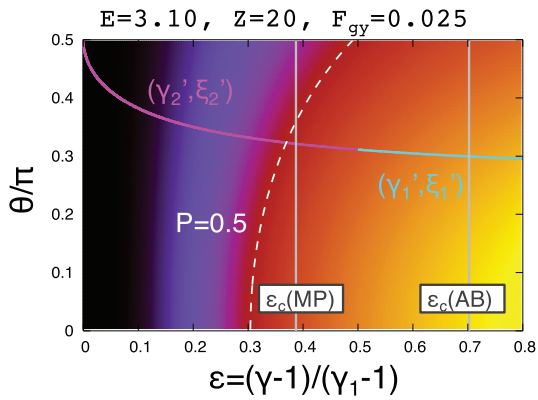


Fig. 6 The runaway probability in the  $(\epsilon, \theta)$  space. The magenta and cyan curves represent the integration path of Eq. (42) for calculating the avalanche growth rate. The vertical segment is  $\epsilon_c = (\gamma_c - 1)/(\gamma_1 - 1)$  obtained by the A-B and MP models, and the dashed curve indicates the contour on which the runaway probability becomes  $\mathcal{P}(\gamma, \theta) = 0.5$ .

observe the same trends  $\Gamma_{\text{avI}}/\Gamma_{\text{RP}} \simeq 1$  for different  $Z$  and the normalized radiation time  $F_{\text{gy}}^{-1}$ . As the second-order collisional diffusion increases the critical energy required for runaways, the A-B model is seen to give lower estimate of the growth rate than the MP model for all cases. Nevertheless, what we can find from Fig. 5 is that the adjoint F-P results overshoot the results of the A-B model and become large even up to the level of the MP model. Comparing Figs. 5 (a) and (b), one can see that the overshoot obtained by the Fokker-Planck method is significant especially at high  $Z$  and low radiation condition. It is consistent with the scan of the critical electric field in Fig. 6 of Ref. [30], where the lower critical threshold as compared to the A-B model prediction has been reported. Here, ‘low radiation’ condition implies lower critical energy for runaways, whereas ‘high  $Z$ ’ implies the enhancement of pitch-angle scattering. For such parameters, the perpendicular scattering due to collisional diffusion [53] becomes significant. Although the collisional diffusion increases the critical energy, as being taken into account by the A-B model, it can simultaneously relax the runaway condition where the smooth transition of runaway probability occurs near the separatrix structure in the momentum space [53]. This interpretation — implying the cancellation of the effect of collisional diffusion — is consistent with our numerical observation of Fig. 5. The avalanche growth rate calculated by the adjoint Fokker-Planck code becomes closer to those obtained by the MP model for intermediate electric fields  $E_{\parallel}/E_{c0} \lesssim 10$ , where the second-order diffusion term is fully truncated.

To compare the A-B and MP models with the adjoint Fokker-Planck method, the contour of the runaway probability  $\mathcal{P}(\gamma, \theta)$  near the sustainment field ( $E_{\parallel}/E_{c0} = 3.10$ ,  $Z = 20$ , and  $F_{\text{gy}} = 0.025$ ) is illustrated in Fig. 6, where we indicate the integration path of the avalanche growth rate in Eq. (42) by magenta and cyan curves for secondary

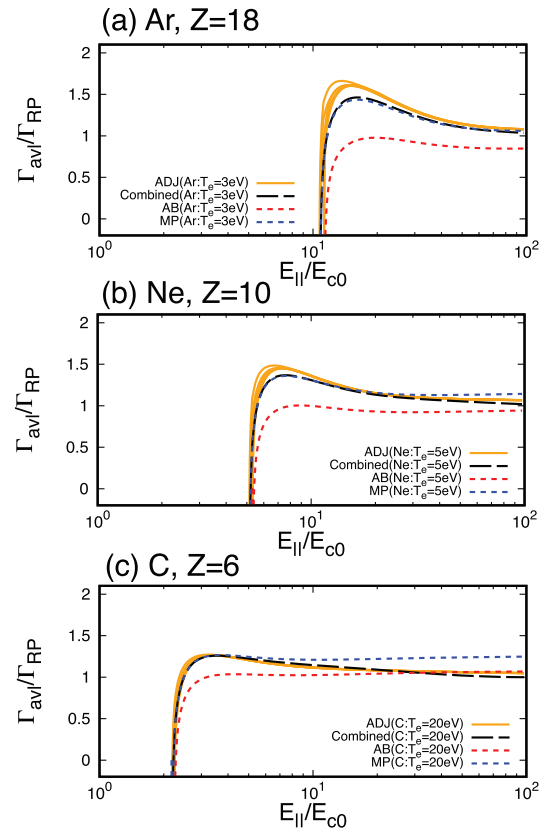


Fig. 7 The same figure with Fig. 5 for different impurity species (Ar, Ne, and C) using the full expression of the impurity collision coefficients  $\alpha_e(q)$  and  $Z(q)$  in Eqs. (17) and (18). The long dashed curves indicate the avalanche growth rate calculated by the combined expression [Eq. (43)] of the MP and R-P models.

and primary electrons, respectively, as well as the contour curve of the probabilities of runaway and loss being equal,  $\mathcal{P}(q, \theta) = 0.5$ . We see that the  $\mathcal{P}(q, \theta) = 0.5$  curve is in reasonable agreement with the runaway separatrix  $\epsilon_c$  obtained by the MP model. In this case, we see that the  $\epsilon_c$  obtained by the A-B model is located on the right of the  $\mathcal{P}(q, \theta) = 0.5$  contour, which gives a negative growth rate, following Eq. (6). On the contrary, it is clear from Fig. 6 that when calculating the avalanche growth rate of Eq. (42), the positive contribution from the first term, representing that secondary electrons run away, tends to dominate over the negative one from the second term, representing the momentum loss of primary electrons. Such an asymmetry would also be attributed to the fact that the perpendicular diffusion is more effective for secondary electrons with lower energies and larger pitch angles  $\xi \simeq 0$  than for primary electrons.

In Fig. 7, another benchmarking of the growth rate with the full expression of the impurity collision model,  $\alpha_e(q)$  and  $Z(q)$  in Eqs. (17) and (18), has been illustrated for three different species (Ar, Ne, and C). Note here that in Fig. 7, the same normalization with  $E_{c0}$  is applied to the  $x$ -axis, the shift of the critical electric field  $\Gamma_{\text{avI}}(E_{\parallel}) \rightarrow -\infty$

is attributed not only to the synchrotron radiation but also the bounded-electron friction. Motivated by the aforementioned comparison, we introduce a combined model that smoothly connects the MP model and the strong electric field limit of the R-P one:

$$\Gamma_{\text{avl}}(\bar{E} > 1) = \Gamma_{\text{MP}} \exp[-\beta(\bar{E} - 1)] + \Gamma_{\text{RP}}\{1 - \exp[-\beta(\bar{E} - 1)]\}, \quad (43)$$

where  $\Gamma_{\text{MP}}$  is the growth rate obtained from Eq. (6) with the critical energy of the MP model, and  $\Gamma_{\text{RP}}$  is obtained from the linear expression of Eq. (3). In Eq. (43),  $\bar{E} = E_{\parallel}/E_c^*$  denotes the normalized electric field, whereas the fitting coefficient is selected to be  $\beta \approx 0.1$ . In Fig. 7, we see that the combined expression of Eq. (43) has reasonably reproduced the results of the adjoint Fokker-Planck method. Such a simple model is useful for a fast evaluation of the growth rate in simulations, instead of solving the Fokker-Planck equation. (The similar idea has also been proposed in Ref. [54].)

## 5. Zero-Dimensional CQ Simulation with Low-Z and Noble Gas Species

### 5.1 ITER simulations with argon injection

In this section, we implement the developed models for impurity collisions and the avalanche growth rate into a 0D CQ simulation. We first examine the sensitivity of the simulation results to the different models of the avalanche growth rate. A simulation is performed for the ITER-relevant parameter with argon impurity, where the device parameters are chosen to be  $R_0 = 6.2$  m,  $a = 2$  m,  $B_0 = 5.3$  T,  $\kappa = 1.8$ , and  $I_p = 15$  MA. With the density of bulk hydrogen  $n_H = 1 \times 10^{20}/\text{m}^3$  for the electron temperature  $T_e = 3$  eV, the required argon density for the power balance is estimated to be  $\approx 2 \times 10^{20}/\text{m}^3$ . For the sake of simplicity, we calculate the power balance only at once and the time variation of the electron temperature during CQ is not taken into account. In this section, the initial seed current is simply given as constant input parameter with  $I_{\text{seed}} = 0.1$  A.

Figure 8 compares the simulation results based on the near-critical threshold theory using the A-B and MP models with those obtained by the R-P model, where we have also performed the simulation turning off the bremsstrahlung term in Eq. (35). Each subfigure corresponds to (a) the time history of the RE currents, (b) the electric field, (c) the avalanche growth ( $\Gamma_{\text{avl}} > 0$ ) and damping ( $\Gamma_{\text{avl}} < 0$ ) rates, and (d) the history of unstable ( $\gamma_c$ ) and stable ( $\gamma_1$ ) roots of the momentum-space flow calculated by the A-B and MP models. Using the near-critical threshold theory, the INDEX simulation has reasonably reproduced the expected behavior of the runaway current and the electric fields near the critical threshold [25]. After the maximum RE current builds up, the RE current slowly damps with the momentum loss due to close colli-

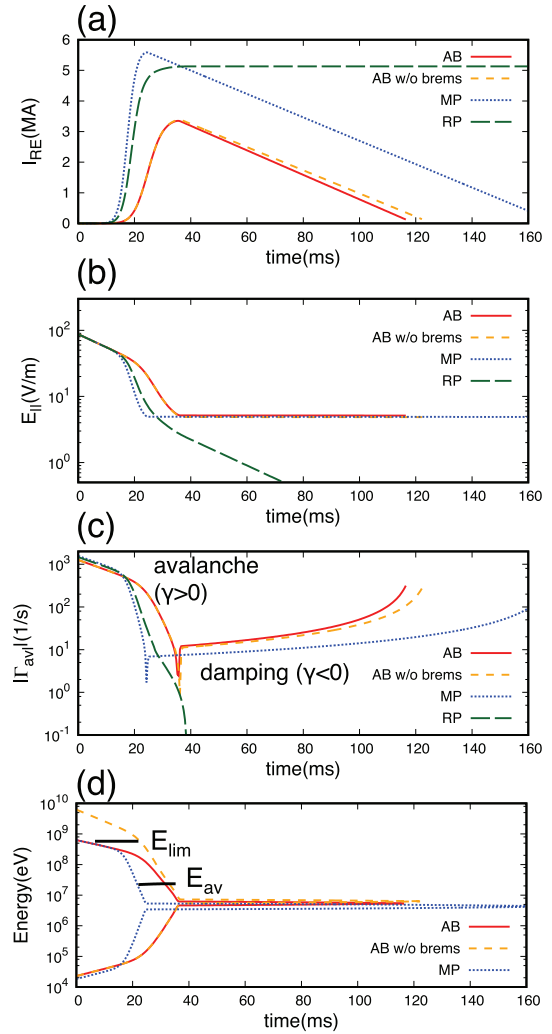


Fig. 8 The time history of (a) the runaway currents, (b) the electric field, (c) the avalanche growth ( $> 0$ ) and collisional damping ( $< 0$ ) rates  $|\Gamma_{\text{avl}}| = |d \log n_{\text{RE}}/dt|$ , and (d) the unstable ( $\gamma_c$ ) and stable ( $\gamma_1$ ) roots for the momentum-space flow.

sions between primary electrons and thermal ones. Such a decaying process is compared in Fig. 8 (a). The RE current predicted by the MP model exhibits a longer sustainment time because higher maximum current is dissipated. Figure 8 (c) shows that except the final termination phase of the RE currents, the collisional damping rate obtained by the A-B and MP models are in agreement within the accuracy of factor 2, where the electric field is sustained around  $\approx 50$  V/m for the both models in Fig. 8 (b). Two important characteristic energies are compared with the energy limit in Fig. 8 (d). The upper one is the maximum attainable energy of runaway electrons calculated from the total available poloidal flux,  $E_{\text{lim}} \lesssim \frac{ec}{2\pi R_0} L_p I_p$  for accelerating the electrons. As is seen from the high energy root  $\gamma_1$  in Fig. 8 (d), the effect of bremsstrahlung appears as a mechanism determining the energy limit, nevertheless, which is less pronounced because  $E_{\text{lim}}$  can limit the runaway energy much lower than the levels where the bremsstrahlung

becomes important. In Fig. 8 (d), the average energy of secondary electrons  $E_{av} = \frac{W_{RE}}{N_{RE}} \approx m_e c^2 a(Z) \ln \Lambda$  is also plotted, where  $N_{RE} = 2\pi R_0 I_{RE} / ec$  is the total number of runaway electrons. The corresponding stored energy  $W_{RE}$  is calculated from the R-P model as [6, 31, 32]

$$\begin{aligned} W_{RE}(t) &= 2\pi R_0 \int dt I_{RE}(t) E_{||}(t) \\ &= - \int_{\psi_0}^{\psi} I_{RE}(t) d\psi \\ &= \psi_A a(Z) \ln \Lambda (I_{RE}(t) - I_{seed}). \end{aligned} \quad (44)$$

The resultant electron distribution function is predicted to have an exponential form characterized by the effective temperature  $\sim \exp(-E/E_{av})$  [6], where  $E$  is the kinetic energy of runaway electrons. The ratio between the magnetic energy  $W_m \approx \frac{1}{2} \mu_0 R_0 I_{RE}^2$  to the kinetic energy is obtained as  $W_m / W_{RE} \approx I_{RE} / [I_A a(Z) \ln \Lambda] \gg 1$  [55]. This is an important ordering that validates the present framework based on the coupling of REs with a bulk plasma only through the runaway current (magnetic energy). Under this assumption, although the conversion of the magnetic energy to kinetic energy is normally retained, the dissipation of kinetic energies of REs, e.g., due to synchrotron radiation, is neglected in the CQ modeling [Eq. (1)] and the power balance relation [Eq. (14)].

Figure 9 (a) compares the dependence of the maximum current  $I_{RE,max}$  (obtained before the collisional damping starts) on the impurity atom density. Here, the vertical segments ( $E_{||}/E_c \approx 50$ ) at  $n_{Ar} \approx 10^{20}/m^3$  roughly characterizes the transition from the strong avalanche regime ( $E_{||}/E_c^* \approx 10^2$ ) to the weak electric field ( $E_{||}/E_c^* \approx 5-10$ ). According to the benchmark in Sec. 4.3, in the strong avalanche regime with the argon density of  $10^{18} - 10^{20}/m^3$ , the  $Z$  dependence of the R-P model is expected to be reliable. In the regime of  $n_{Ar} \gtrsim 10^{20}/m^3$ ,  $I_{RE,max}$  decreases with the argon density, where the MP model can be regarded as a reasonable prediction that can reproduce the results of the Fokker-Planck code. The necessary density for the RE suppression [2] is observed similarly at  $n_{Ar} \approx 10^{21}/m^3$  with these three models. The  $n_{Ar}$  dependence of the collisional damping rates is summarized in Fig. 9 (b), showing good agreement between the different models of the avalanche growth rate. The effect of the bremsstrahlung radiation is seen to be negligible in both net RE production and the collisional damping rate.

A possible mitigation scheme of the RE production, as compare to the pure argon injection like Fig. 9, is to increase the bulk ion (deuterium) density. Figure 10 compares the maximum RE current  $I_{RE,max}$  in the same way with Fig. 9 for two different bulk-ion densities,  $n_H = 1 \times 10^{20}$  and  $4 \times 10^{21}/m^3$ , the latter corresponding to the amount on the order that is expected for massive deuterium injection ( $\approx 12.8 \text{ kPa} \cdot m^3$  with the volume  $800 \text{ m}^3$ ). Here we compare the prediction obtained by the standard R-P model with those obtained from the combined one of

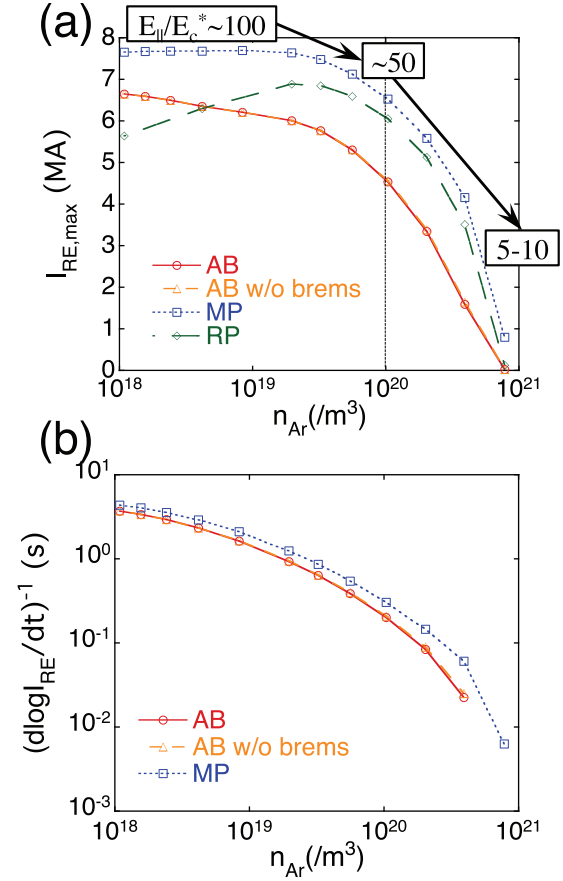


Fig. 9 (a) Maximum RE current for ITER simulations with argon impurity and  $I_{seed} = 0.1 \text{ A}$ . (b) The lifetime of RE current  $(d \log(I_{RE})/dt)^{-1}$  (s).

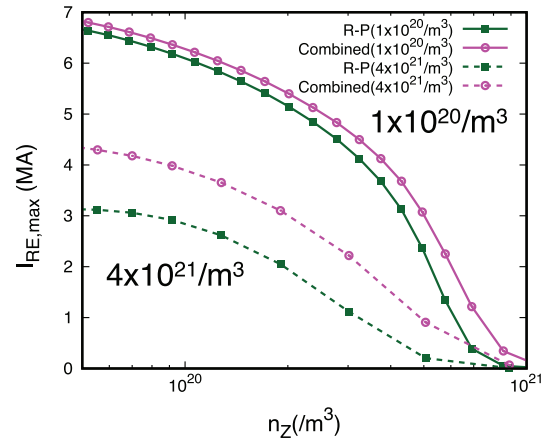


Fig. 10 Comparison of the maximum RE current calculated by the R-P model [Eq. (2)] and the combined model [Eq. (43)] for two different bulk ion density:  $n_H = 1 \times 10^{20}$  and  $4 \times 10^{21}/m^3$ .

Eq. (43), taking into account the cancellation of the collisional diffusion, which has been discussed in the previous section. Figure 10 shows that a close prediction between the combined and R-P models is obtained for the

low density case. Conversely, for the high density case, because the electric field decreases to the level of the intermediate electric field  $E_{\parallel}/E_c^* \simeq 10$ , net RE production obtained from the combined expression (magenta) becomes significantly larger than those from the R-P model (green). The comparison of Fig. 10 has illustrated that the modeling accuracies including the cancellation of the collisional diffusion become important for lower normalized electric fields, thus being useful for the quantification of runaway mitigation.

## 5.2 Comparison of low- $Z$ and noble gas species

Next we compare the RE production in the presence of different impurity species. We perform the simulation using the parameters relevant to JT-60U and JET-size, with a relatively high pre-disruption plasma current to drive the avalanche growth, where  $I_p = 4$  MA,  $R_0 = 3$  m,  $a = 1$  m,  $B_0 = 3$  T,  $\kappa = 1.6$ , and  $n_H = 1 \times 10^{20}/\text{m}^3$ . Let us consider Be ( $Z = 4$ ) and C ( $Z = 6$ ) as representative species for intrinsic impurities in natural disruptions, and Ar ( $Z = 18$ ) and Ne ( $Z = 10$ ) for mitigated disruptions. To calculate the avalanche growth rate, we have used the the combined semi-analytic model of Eq. (43).

Figure 11 shows the 2D map of the maximum runaway current  $I_{RE,max}$  for (a) beryllium, (b) carbon, and (c) argon impurity with  $I_{seed} = 1$  kA. The same calculation for neon is qualitatively similar to those of argon. The RE current appears in the 2D map of Fig. 11 is determined by two dominant physics: (1) the electric field increases with the resistivity through the change of the electron temperature and  $Z_{eff}$ , and (2) at high  $n_Z$  with low  $T_e$ , the bounded electron enhances the electron friction through  $\alpha_e$  and contributes to the RE suppression. In Fig. 11, white curves indicate the power balance between the ohmic and radiation losses. TQ should occur along any trajectory passing the region above the power balance curve if one neglects the effect of transport losses on the electron temperature. After TQ, the operational point will reach to some stable equilibrium point, characterizing the plasma parameter during CQ at the power balance.

The above picture of the power balance analysis is useful to interpret the parametric dependence of RE generation on the impurity content during CQ. In Fig. 12, we have evaluated the fraction of  $I_{RE,max}$  to the pre-disruption plasma current along the power balance curve for three different values of the seed current,  $I_{seed} = 0.1, 1, 10$  kA. When the multiple root exists, the solid curve is used only for a stable root at high temperature side (more easily accessible). In such a way, the threshold impurity density separating the two distinct regions having weak and strong avalanche growth rates is obtained for low- $Z$  materials. Comparing beryllium and carbon in Figs. 12(a) and (b), we see that the strong avalanche regime is accessible with smaller amount of the carbon impurity ( $n_C \gtrsim 1 \times 10^{20}/\text{m}^3$ )

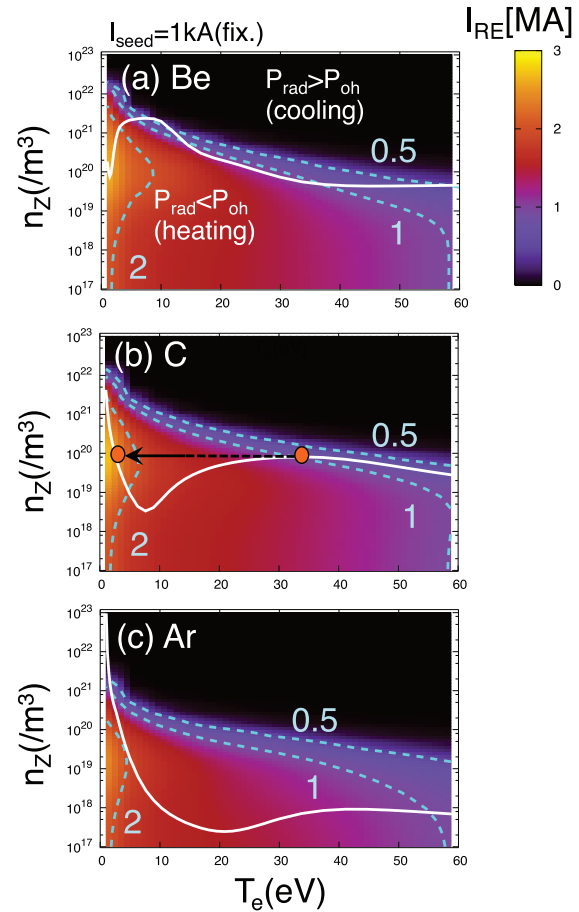


Fig. 11 Maximum RE current  $I_{RE,max}$  calculated by the INDEX code in the  $(T_e, n_Z)$  space for (a) Be, (b) C, and (c) Ar injection. The power balance between the ohmic heating and the radiation loss is indicated by white curves. In (b), the onset of strong avalanche regime with the access to the low  $T_e$  equilibrium point is indicated by the arrow.

than that of beryllium ( $n_{Be} \gtrsim 2 \times 10^{21}/\text{m}^3$ ). In Figs. 12(c) and (d), the same work has been done for noble gas species. Both for argon and neon injection, the regime with strong avalanche growth rate is accessible with lower atom densities ( $n_{Ar} \gtrsim 10^{18}/\text{m}^3$  and  $n_{Ne} \gtrsim 10^{19}/\text{m}^3$ ) than that is necessary for low- $Z$  materials, though in the case of argon, the two regimes are almost connected continuously. This threshold density depends mainly on the impurities species and weakly on the current density as the power balance curve is. As is seen from the results of Fig. 12, the seed current does not affect the thresholds but once the impurity content exceeds them, the net RE production is varied with the seed current on a logarithmic scale.

In Fig. 13, the electric field at the beginning of CQ ( $t = 0$ ) is normalized by the critical threshold  $E_c^*$ , and is plotted as a function of the impurity density. Other than quantitative details, all the species exhibit a similar trend: indicating that just above the onset, the maximum normalized electric field on the order of  $E_{\parallel}/E_c^* \sim 10^2$  is

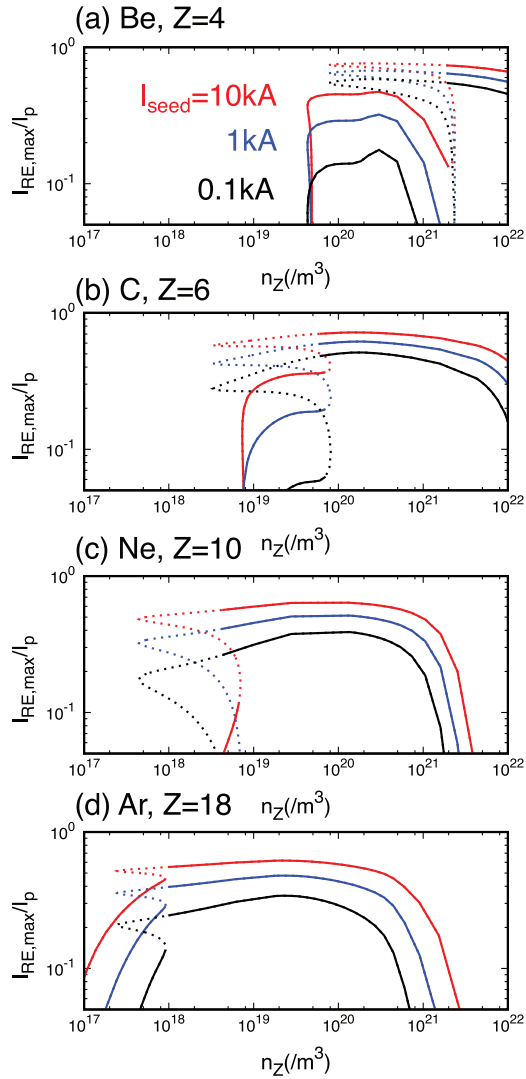


Fig. 12 The fraction of the produced RE current to pre-disruption plasma current  $I_{RE,max}/I_p$  evaluated along the power balance curve of Fig. 11, as function of the impurity atom density. We have used the solid curve only for a stable root at high temperature side (more easily accessible) if the multiple roots exist. Three different curves indicate the results obtained with the different seed currents:  $I_{seed} = 10$  kA (red), 1 kA (blue), and 0.1 kA (black).

available. With increasing the impurity density above the threshold, the normalized electric field decreases, implying the mitigation of avalanche growth at the high impurity density regime. Such a mitigation is attributed to the enhancement of the bounded-electron friction force. Comparing to such pure injection, we examine the effect of the background ion density. In Fig. 14, (a) the normalized electric field  $E_{||}/E_c^*$ , (b) the critical energy required for runaways, and (c) the produced RE current  $I_{RE,max}$  are illustrated for neon ( $Z = 10$ ) with five different ion density ( $n_H = 1 \times 10^{20}$ ,  $5 \times 10^{20}$ ,  $1 \times 10^{21}$ ,  $2 \times 10^{21}$  and  $4 \times 10^{21}/m^3$ ). Here the seed current is fixed at  $I_{seed} = 1$  kA in Fig. 14(c),

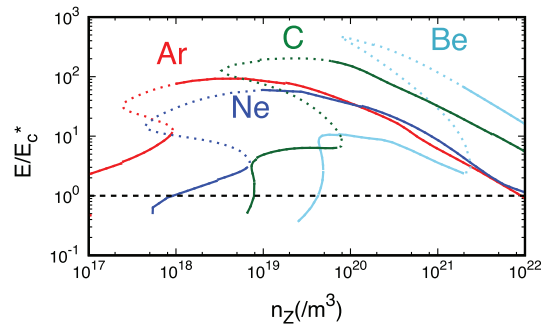


Fig. 13 The impurity density dependence of the ratio of the electric field at the beginning of CQ ( $t = 0$ ) to the critical electric field  $E_c^*$  for different species (Be, C, Ne, and Ar).

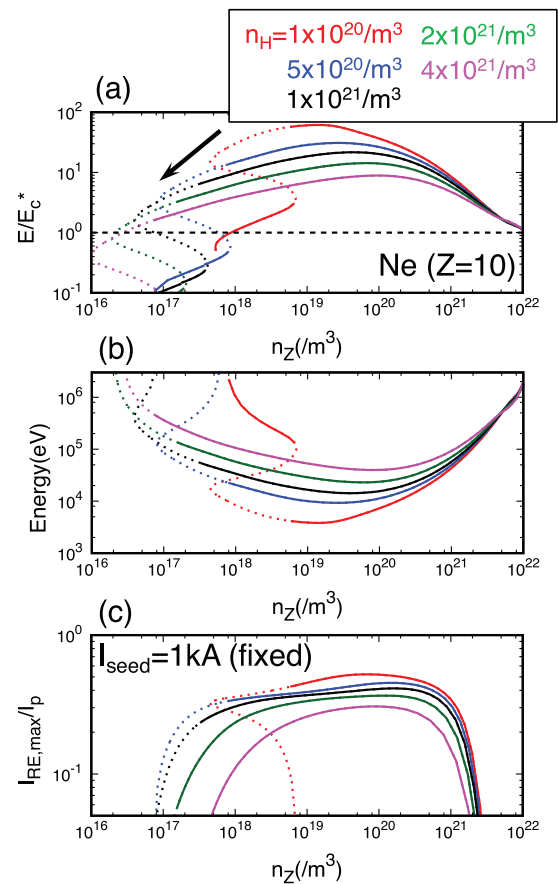


Fig. 14 (a) The same figure with Fig. 13 for neon with five different bulk ion densities: (red)  $n_H = 1 \times 10^{20}/m^3$ , (blue)  $5 \times 10^{20}/m^3$ , (black)  $1 \times 10^{21}/m^3$ , (green)  $2 \times 10^{21}/m^3$ , and (magenta)  $4 \times 10^{21}/m^3$ . (b) The critical energy required for runaways,  $(\gamma_c - 1)m_e c^2$ . (c) The fraction  $I_{RE,max}/I_p$  of the produced RE current to pre-disruption plasma current.

thus indicating the capability of secondary runaway generation. Since the radiation loss is enhanced with the electron density, the threshold neon density shifts to the left as indicated by the arrow in Fig. 14(a), decreasing with the

increase of the background ion density. (It implies that the neon are replaced by bulk ions.) Simultaneously, the normalized electric field  $E_{\parallel}/E_c^*$  decreases to the range of  $E_{\parallel}/E_c^* \lesssim 10$ , which is beneficial to reduce the primary electron generation through the increase of the critical energy required for runaways by up to an order of the magnitude. Nevertheless, the reduction of secondary electron generation with the fixed seed current is not so significant, being less than a factor of 2 at  $n_Z = 10^{19} - 10^{20}/\text{m}^3$ , as is seen by Fig. 14 (b). This is because the increase of the background electron density and the decrease of the effective  $Z$  counteracts to the reduction of the avalanche growth rate due to the lower normalized electric field.

## 6. Zero-Dimensional TQ Simulation for Hot-Tail Generation

The analysis in the previous section — for the avalanche growth with given seed currents — must be complemented by self-consistent evaluation of the seed currents. This is a more complicated problem because seed currents are affected by the physics on the timescale of TQ and are sensitive to dynamic changes of the plasma parameters during disruptions. This section describes the development of 0D TQ simulations using the INDEX code, which consists of the rate equations and the energy balance equations without assuming the ionization equilibrium. This is an original motivation of a charge-resolved implementation of the INDEX code, similarly to what is done in the DIMRUN code [56], although the opacity effect in Ref. [56] is out of the scope of this work. In Sec. 6.2, the developed TQ model is coupled to the Fokker-Planck code for evaluating hot-tail seed electrons. To account for the drag force due to cold electrons produced by ionization of the impurity neutrals, a two-temperature electron model is considered.

### 6.1 Radiative cooling and power balance

In the INDEX code, the ionization and recombination processes during TQ are solved in terms of the rate equations. For impurity ions of the species  $s$  with the charge state  $j+$ , the evolution of the density equation  $n_s^{j+}$  is written by

$$\begin{aligned} \frac{\partial n_s^{j+}}{\partial t} = & S_s^{(j-1)+} n_e n_s^{(j-1)+} - (S_s^{j+} + \mathcal{A}_s^{j+}) n_e n_s^{j+} \\ & + \mathcal{A}_s^{(j+1)+} n_e n_s^{(j+1)+} + \delta_{j,0} S_n^0, \end{aligned} \quad (45)$$

where  $S_s^{j+}$  and  $\mathcal{A}_s^{j+}$  are the ionization and recombination coefficients [57]. In Eq. (45), the neutral source is given by  $S_n^0 = \Delta n_s^0 / \tau_{\text{source}} H(\tau_{\text{source}} - t)$ , where  $\Delta n_s^0$  denotes the injected density,  $\tau_{\text{source}}$  characterizes the deposition time, and  $H(t)$  denotes the step function.

When a large amount of the impurity neutrals are deposited and ionized in a plasma, cold electrons are released, and the temperature relaxation occurs between the

cold and hot populations [18]. To simulate such a relaxation process, we treat the density of cold electrons  $n_{ce}$  with the temperature  $T_{ce}$ , which is released from impurity neutrals, as an independent species that is separated from pre-existing hot one  $n_{he}$  with the temperature  $T_{he} (> T_{ce})$ . In our simulations, the relaxation between cold and hot electrons is treated using the particle source term for the equation of hot-electron density  $n_{he}$ :

$$\frac{\partial n_{he}}{\partial t} = S_{he,ce}^{\text{ex}}, \quad S_{he,ce}^{\text{ex}} \equiv \frac{2P_{he,ce}^{\text{ex}}}{3T_{he}}. \quad (46)$$

Here, the source rate is written in terms of the power transfer between the species  $\alpha$  and  $\beta$  [58]

$$\begin{aligned} P_{\alpha,\beta}^{\text{ex}} &= \frac{3n_{\alpha}(T_{\beta} - T_{\alpha})}{2\tau_{\alpha\beta}}, \\ \tau_{\alpha\beta} &= \frac{3\sqrt{2}\pi^{3/2}\epsilon_0^2 m_{\alpha} m_{\beta} \left(\frac{T_{\alpha}}{m_{\alpha}} + \frac{T_{\beta}}{m_{\beta}}\right)^{3/2}}{n_{\beta} e^4 Z_{\alpha}^2 Z_{\beta}^2 \ln \Lambda_{\alpha\beta}}, \end{aligned} \quad (47)$$

where the Coulomb logarithm  $\ln \Lambda_{\alpha\beta}$  is evaluated using the formula of Ref. [59]. The density of cold electrons is obtained from the quasi-neutrality  $n_{ce} = \max(0, n_H + \sum_s \sum_j Z_s^{j+} n_s^{j+} - n_{he})$ , where  $n_H$  denotes fully-ionized bulk hydrogen density. After the temperature equilibration between cold and hot electrons is finished, we no longer solve Eq. (46), and the hot-electron density is obtained as  $n_{he} = n_H + \sum_s \sum_j Z_s^{j+} n_s^{j+}$ . As we will see below, Eq. (46) can be incorporated into the Fokker-Planck code as the source term, being useful for taking into account the electron density variation during TQ.

The energy balance equations are given in terms of the pressure  $p_s = n_s T_s$  for each component, as being written by

$$\begin{aligned} \frac{\partial}{\partial t} \left( \frac{3}{2} p_{he} \right) &= P_{he,ce}^{\text{ex}} + P_{he,H}^{\text{ex}} + \sum_s P_{he,s}^{\text{ex}} \\ &+ P_{OH} - P_{ion}^{\text{he}} - P_{rad}^{\text{he}} - \frac{3}{2} T_{he} S_{he,ce}^{\text{ex}}, \end{aligned} \quad (48)$$

$$\begin{aligned} \frac{\partial}{\partial t} \left( \frac{3}{2} p_{ce} \right) &= P_{ce,he}^{\text{ex}} + P_{ce,H}^{\text{ex}} + \sum_s P_{ce,s}^{\text{ex}} \\ &- P_{ion}^{\text{ce}} - P_{rad}^{\text{ce}} + \frac{3}{2} T_{he} S_{he,ce}^{\text{ex}}, \end{aligned} \quad (49)$$

$$\frac{\partial}{\partial t} \left( \frac{3}{2} p_H \right) = P_{H,he}^{\text{ex}} + P_{H,ce}^{\text{ex}} + \sum_s P_{H,s}^{\text{ex}}, \quad (50)$$

$$\frac{\partial}{\partial t} \left( \frac{3}{2} p_s \right) = P_{s,he}^{\text{ex}} + P_{s,ce}^{\text{ex}} + P_{s,H}^{\text{ex}}, \quad (51)$$

where  $P_{OH} = \eta(j_{\parallel} - j_{RE})^2$  denotes the ohmic heating, and  $P_{ion}^{\text{he/ce}}$  and  $P_{rad}^{\text{he/ce}}$  denote the ionization and radiation losses. In Eq. (51), we assume that different charge states of the impurities have an equal temperature  $T_s$ . The last term in Eq. (48) [Eq. (49)] is subtracted (added) to compensate the energy exchange results from the particle transfer of Eq. (46). Note that the ohmic heating power is added only to hot components, since the current is carried by a medium with the higher conductivity, and the power balance with

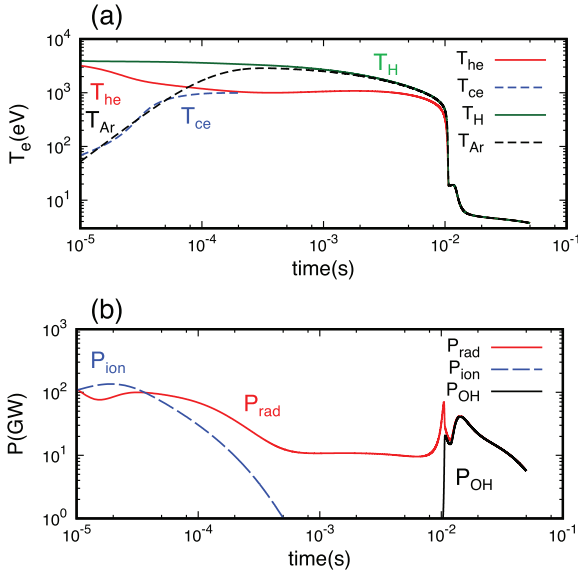


Fig. 15 (a) The evolution of the temperature of hot electrons ( $T_{he}$ ), cold electrons ( $T_{ce}$ ), bulk ions ( $T_H$ ), and argons ( $T_{Ar}$ ). (b) The ohmic heating and radiation and ionization loss powers. The pre-TQ parameters are chosen to be  $T_{he} = 4$  keV,  $n_H = 10^{20}/\text{m}^3$ ,  $j_0 = 0.75$  MA/m<sup>2</sup>, and  $\Delta n_{Ar}^0 = 1.3 \times 10^{19}/\text{m}^3$ .

the radiation loss is achieved only at the final phase of TQ. To evaluate the ohmic heating power and the associated electric field (Ohm's law) for a multi-species plasma, the classical resistivity is obtained using the matrix inversion [60] in terms of the friction coefficient of Ref. [61].

Figure 15 illustrates (a) the temperature relaxation between the electron and ion species and (b) the history of heating and loss powers. In the simulation of Fig. 15, the initial condition is chosen to be  $T_{he} = T_H = 4$  keV with  $n_H = 10^{20}/\text{m}^3$  and  $Z_{\text{eff}} = 1$ , and the argon density  $\Delta n_{Ar}^0 = 1.3 \times 10^{19}/\text{m}^3$  is introduced as neutrals at  $t = 0$ , i.e.,  $\tau_{\text{source}} \rightarrow 0$  in Eq. (45). The temperature evolution of Fig. 15 (a) shows that on the short timescale of  $10^{-5}$ – $10^{-4}$  s after the impurity injection ( $t = 0$ ), the hot electron population ( $T_{he}$ ) cools down due to dilution. The two-temperature model has an advantage at this point where we do not need to assume that the heating time of cold electrons is much faster than the production time of cold electrons. Next, in Fig. 15, we see that the electron temperature drop due to dilution is followed by the temperature equilibration with ions (H+Ar) and by slow cooling with bremsstrahlung and line radiation. In the present case, the radiative collapse occurs at  $t \approx 10^{-2}$  s, and a plasma immediately reaches the final temperature around a few eV. As seen from Fig. 15 (b), the power balance between the ohmic heating and the radiation loss is achieved at the final point of TQ. The resultant plasma parameters ( $T_e$ ,  $n_{he}$ , and  $Z_{\text{eff}}$ ) at the power balance has been cross-checked with a direct evaluation of the power balance equation from Eq. (14).

## 6.2 Hot-tail electron production during massive Ar injection

Various mechanisms have been considered [9] as the cause of primary (seed) electrons that triggers the avalanche amplification in ITER-grade devices. During the rapid plasma cooling, being relevant to rapid shut-down scenarios like the massive gas injection, the incomplete thermalization of the electron distribution function yields hot-tail seeds [10–18]. To simulate the hot-tail generation during TQ, an initial-value Fokker-Planck routine is coupled self-consistently to the 0D TQ simulations of the INDEX code. In our simulations, the Fokker-Planck code is used to follow the distribution function of hot electron (he) populations. The relativistic Fokker-Planck equation in the high-velocity limit [Eq. (25)] is replaced by its weak relativistic form of Ref. [62] to include the finite temperature effect. Note that the finite temperature correction, namely,  $O(\epsilon)$  terms in Eq. (5) of Ref. [62], is included only for describing collisions with hot and cold electrons, whereas we still apply the high-velocity limit to the friction coefficients due to ions and bounded electrons.

In simulations, the Fokker-Planck code and the TQ model are solved self-consistently without assuming any scale separation, where the friction coefficients in the Fokker-Planck equations are updated with time, following the density and temperature evolutions obtained by the TQ model. To take into account the evolution of hot-electron densities  $n_{he}$ , the source term based on Eq. (46) has been implemented to Eq. (25) as

$$\tau_0 \frac{\partial f}{\partial t} + \hat{E} \mathbf{b} \cdot \nabla_{\mathbf{q}} f = C(f) + C_s(f) + C_B(f) + \frac{d \ln n_{he}}{dt} f_M, \quad (52)$$

where  $f_M(v) = n_{he}/(\pi^{3/2} v_T^3) \exp[-(v/v_T)^3]$  represents a Maxwellian distribution function with the thermal velocity  $v_T = \sqrt{2T_{he}/m_e}$ . Using the time dependent solutions of Eq. (52), the hot-tail seed current is evaluated as  $j_{\text{seed}}^{\text{hot-tail}} = \int_{q > q_c} d^3 \mathbf{q} c q_{\parallel} f(q, \theta) / \gamma$ , where  $q_c = \sqrt{\gamma_c^2 - 1}$  denotes the critical momentum. The electric field that accelerates electrons is evaluated self-consistently from the Ohm's law,  $E_{\parallel} = \eta(j_{\parallel} - j_{RE})$ , where we assume that the density of runaway electrons is much lower than that of Maxwellian electrons, so that the heating of background electrons by the RE component has been neglected. Note that in our TQ model, the energy exchange between hot and cold (Maxwellian) electrons has already been retained by Eqs. (48) and (49). In Fig. 16, the formation of the beam-like runaway distribution function during TQ has been illustrated. The physics behind the transformation from the nearly isotropic distribution to the beam-like distribution has been discussed in Ref. [18]. Figure 17 illustrates the dependence of hot-tail seed currents on the injected argon density for seven different pre-TQ temperature in the range from 2 keV to 8 keV, where the instantaneous deposition of impurities is assumed with  $\tau_{\text{source}} = 0.01$  ms. Including

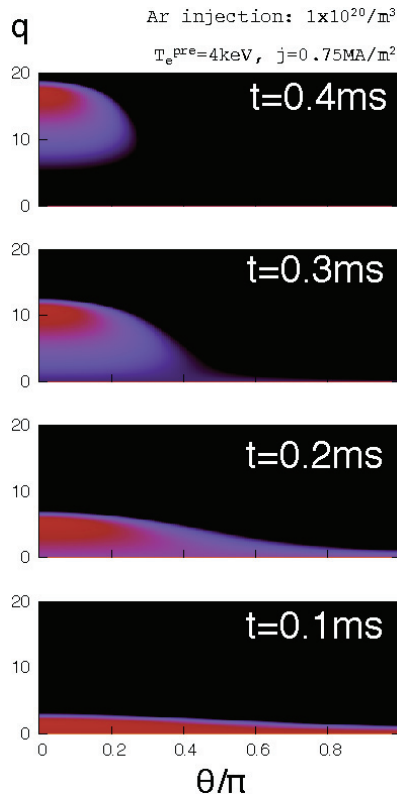


Fig. 16 Formation of beam-like distribution function during TQ (the contour in the space of normalized momentum  $q$  vs. the pitch angle  $\theta$ ). The simulation parameters are  $j = 0.75 \text{ MA/m}^2$ ,  $T_{\text{he}}^{(\text{pre})} = T_{\text{H}} = 4 \text{ keV}$ ,  $\Delta n_{\text{Ar}}^0 = 1 \times 10^{20}/\text{m}^3$ , and  $\tau_{\text{source}} = 0.05 \text{ ms}$ .

a non-monotonic dependence on the pre-TQ temperature, being significant around 2 keV, the simulation results of Fig. 17 have well reproduced a quantitative trends that is observed in Fig. 5 (a) of Ref. [18].

In comparison to the previous work [18], solving the rate equation is computationally demanding but detailed history of the impurity ionization can be retained in our simulations. In Fig. 18, the hot-tail generation is simulated for five different values (0.01, 0.03, 0.1, 0.3, and 1 ms) of the deposition time  $\tau_{\text{source}}$  of impurity neutrals. Due to the complicated electron temperature dependence of radiation and ionization, the evolution of the electron temperature and the runaway seed current exhibit no simple dependence on the initial conditions. Here we observe a counter-intuitive example in Fig. 18 (b) where the smaller amount of hot-tail seeds are obtained with the fast deposition of impurity neutrals for  $\tau_{\text{source}} = 0.03$  and 0.01 ms than in the case of the slow deposition,  $\tau_{\text{source}} = 0.1$  ms. The calculated  $j_{\text{seed}}^{\text{hot-tail}}$  is summarized in Fig. 19 as a function of  $\tau_{\text{source}}$  for the different pre-TQ temperature (2, 4, 8 keV) and the injected argon density ( $6 \times 10^{19}$ ,  $1 \times 10^{20}/\text{m}^3$ ). To verify the simulation results, we have also applied Eqs. (5) and (19) of Ref. [14] as the model equation for analytically

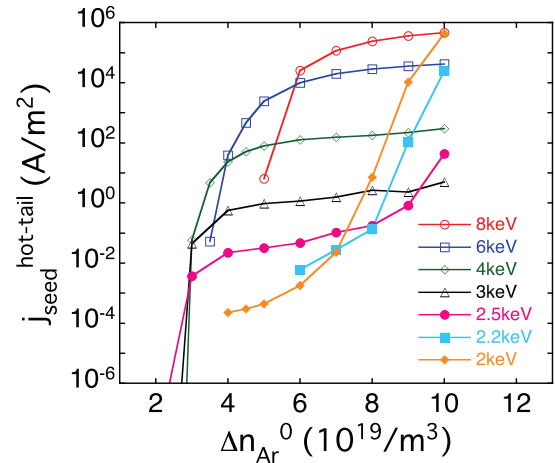


Fig. 17 Dependence of hot-tail seed currents calculated by the Fokker-Planck code on the injected argon density  $\Delta n_{\text{Ar}}^0$  with the current density  $j_0 = 0.75 \text{ MA/m}^2$  and the impurity deposition time  $\tau_{\text{source}} = 0.01 \text{ ms}$ .

evaluating  $j_{\text{seed}}^{\text{hot-tail}}$ . We have confirmed that a qualitative trend can also be captured by the analytic model. The range of  $\tau_{\text{source}}$  considered here corresponds — in the case of the pellet injection — to the order of the pellet ablation time  $r_{\text{pel}}/V_{\text{pel}} \approx 10^{-5} \text{ s}$  and to the lifetime of the pellet  $a/V_{\text{pel}} \approx 10^{-3}$ , where  $r_{\text{pel}}$  is the pellet radius,  $a$  is the plasma minor radius, and  $V_{\text{pel}}$  is the pellet velocity. In Fig. 19, we have also indicated the values of the electron collision time calculated for bulk ( $v = v_{\text{th}}$ ) and hot ( $v = 3v_{\text{th}}$ ) electrons by the triangles on the top and bottom axis. As we expect, the simulation results have shown that when the impurities are slowly deposited on the timescale comparable or slower than the hot-electron collision time (the triangles on the bottom axis), the amount of hot-tail seed currents tends to be smaller by up to the orders of the magnitude. Such a ‘slow’ injection would be a promising way to mitigate the production of hot-tail seeds. For the deposition on the shorter timescale, conversely, we observe that the production of hot-tail seeds becomes significant and the dependence on the pre-TQ temperature and the injected argon density appears to be non-monotonic. The seed current can be comparable at maximum to the pre-disruption plasma current (in this case,  $j_{\parallel} = 0.75 \text{ MA/m}^2$ ), the mechanism being called as the prompt conversion [18]. As a whole, our simulation has shown that the deposition timescale of seed currents is a main factor affecting the hot-tail seed generation, and the dependence of hot-tail seeds on the pre-TQ temperature and the injected argon density exhibits a non-monotonic character, depending on detailed history of the atomic processes during the radiative cooling.

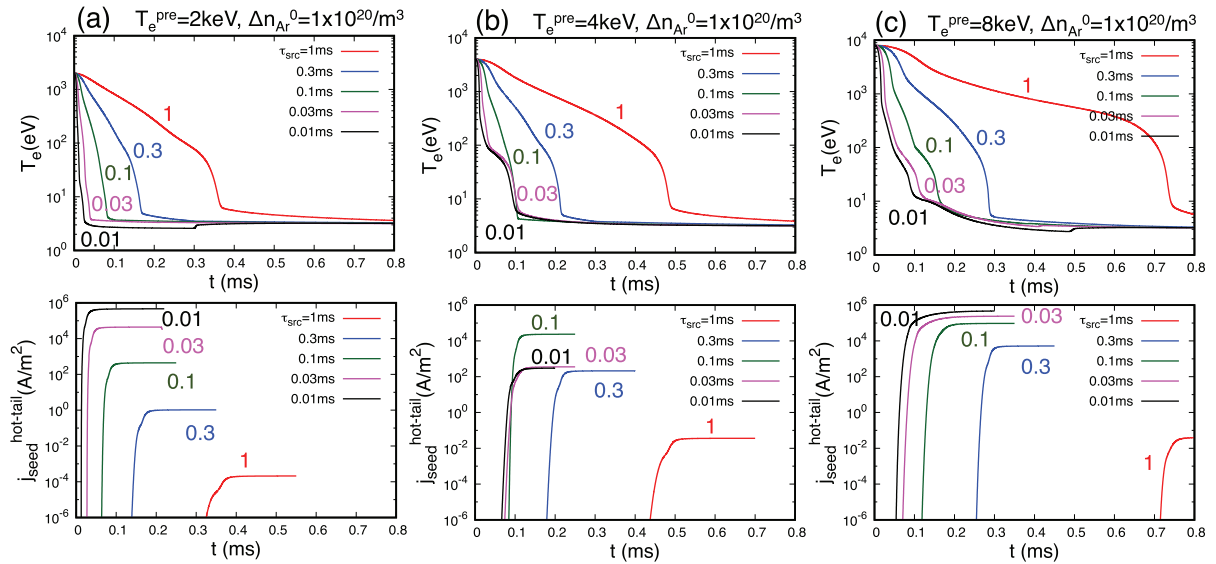


Fig. 18 Time history of the electron temperature (top) and the hot-tail current (bottom) for five different impurity deposition times (1, 0.3, 0.1, 0.03, and 0.01 ms) with  $j = 0.75$  MA/m<sup>2</sup> and  $\Delta n_{\text{Ar}}^0 = 1 \times 10^{20}/\text{m}^3$ : (a)  $T_e^{\text{pre}} = 2$  keV, (b) 4 keV, and (c) 8 keV.

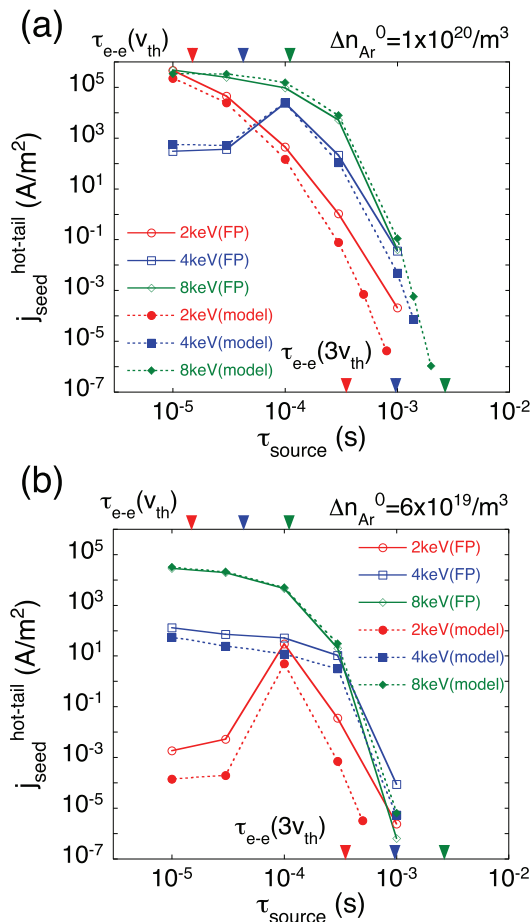


Fig. 19 Dependence of hot-tail seed currents calculated by the Fokker-Planck code (solid) and the model equation by Smith and Verwichte [14] (dashed) on the deposition time  $\tau_{\text{source}}$  of the impurity neutrals for three different pre-TQ temperature (2, 4, 8 keV). The injected argon density is (a)  $\Delta n_{\text{Ar}}^0 = 1 \times 10^{20}/\text{m}^3$  and (b)  $6 \times 10^{19}/\text{m}^3$ .

## 7. Discussion and Conclusion

High impurity content is a key characteristic to understand the generation and mitigation condition of runaway electrons. In this paper, the effects of impurities on runaway generation in a post-disruption plasma have been studied using a zero-dimensional disruption simulation code INDEX. We have focused on its model verification. In ITER, the runaway beam current should be limited less than 2 MA [3], being less than 20% of the full plasma current. This constraints imply that the same degree of accuracy is required for predictive modeling. In the present paper, in addition to the implementation of a charge-resolved expression of the Coulomb logarithm, the different models of calculating the critical energy, the energy limit and the avalanche growth rate have been compared quantitatively, and self-consistent TQ simulation with the hot-tail effect has been developed.

For verifying the calculated avalanche growth rate, we have applied numerical solutions of the adjoint Fokker-Planck equation, which shows that (1) the Fokker-Planck code well reproduces the strong electric field limit ( $E/E_c \gg 1$ ) of the R-P model and its  $Z$  dependence; (2) for the intermediate electric field region ( $E/E_c \lesssim 10$ ) between the sustainment field and the strong electric field limit, favorable effects of second-order collisional diffusion, being retained in the A-B model, are canceled by the relaxation of runaway condition due to its probabilistic nature [53]. Consequently, the avalanche growth rate exceeds the R-P model and becomes close to the prediction by the MP model. Our results are consistent with Fig. 6 of Ref. [29], showing that the lower critical electric field at low radiation and high  $Z$  condition that those obtained from the A-B model. Such modeling accuracies including the cancellation of the collisional diffusion have been shown to become

important for lower normalized electric fields, thus being useful for the quantification of runaway mitigation. As a possible expression that covers arbitrary electric fields, the combined expression that smoothly connects the MP model with the strong electric field limit of the R-P model has been applied to the INDEX code.

Using the developed 0D simulation, we have studied the impurity density required for the onset of strong avalanche amplification. With the aid of the power balance analysis, we have characterized the threshold density separating two distinct regions with weak and strong avalanche growth rates. Just above the onset density, the electric field reaches the level of strong electric field limit of the R-P model,  $E_{||}/E_c^* \approx 10^2$ , therefore, the corresponding Z dependence of the R-P model being dominant for RE production. The threshold density depends on the impurity species and weakly on the current density. The seed current itself does not affect the threshold while once the impurity content exceeds the threshold, the net RE production is varied with the seed current on a logarithmic scale. The deuterium mixing is an effective way to decrease the normalized electric field and increases the critical energy required for runaways. Concerning the dependence on the impurity species, the lower threshold density of Ar and Ne is consistent with the RE production experiments using Ne and Ar pellets in JT-60U [63] and DIII-D [64]. For noble gas species, the avalanche growth rates becomes decreasing with the impurity density above  $10^{20} - 10^{21}/\text{m}^3$ , which is a density range relevant to the massive gas injection (see, Fig. 14 of Ref. [64]). The comparison between Be and C has indicated that the lower threshold density and higher maximum current for C are correlated to the easier production of runaway electrons with carbon wall and are consistent to the comparison between the JET-C and JET-ILW experiments [8].

The above analysis based on given seed currents must be complemented by the self-consistent evaluation of the seed currents. For this purpose, the 0D TQ simulation has been developed for the INDEX code, which is coupled to the relativistic Fokker-Planck code in the weak relativistic form including the friction coefficients due to cold electrons and partially stripped ions. A two-temperature electron model is considered to account for the drag force due to cold electrons produced by ionization of the impurity neutrals. In comparison to the previous work [18], solving the rate equation is computationally demanding but detailed history of the electron cooling, resulting from the ionization, recombination, and radiation processes, can be taken into account. The deposition timescale of impurity neutrals is shown to be a main factor affecting hot-tail seeds, which depend non-monotonically on the pre-TQ temperature and the injected impurity density. Concerning the mitigation of hot-tail seeds, it is clear that ‘slow’ injection on the order of hot-electron collision time is useful to mitigate the hot-tail formation.

In future, further extension of the INDEX code, par-

ticularly, to include 1D profiles is an important step for its application to the runaway mitigation scenario. For this purpose, the coupling of the impurity model developed here to the reduced MHD code [65] will be reported. In such simulations, the interplay with impurity injection process [66–68] and the magnetohydrodynamic (MHD) modes [69, 70] would be important. Additionally, although this work simply assumes that the RE distribution function is identical to monoenergetic one at the energy limit, full kinetic simulations are available in the present framework that couples the initial-value Fokker-Planck code and TQ/CQ simulations. Such simulations improve the prediction of avalanche growth rate near the sustainment fields, and are useful for the direct comparison of the runaway distribution function with the experimental observation [71].

## Acknowledgments

One of the authors (AM) would like to express his gratitude to Drs. N. Aiba, K. Hoshino, and M. Honda for useful discussion. This work was supported in part by Grants-in-Aid for Scientific Research (MEXT KAKENHI Grant No. 26820404 and 17K14904).

- [1] M. Sugihara *et al.*, Nucl. Fusion **47**, 337 (2007).
- [2] M. Lehnen *et al.*, J. Nucl. Mater. **463**, 39 (2015).
- [3] E.M. Hollmann *et al.*, Phys. Plasmas **22**, 021802 (2015).
- [4] Yu. A. Sokolov, JETP Lett. **29**, 218 (1979).
- [5] R. Jayakumar *et al.*, Phys. Lett. A **172**, 447 (1993).
- [6] M.N. Rosenbluth and S.V. Putvinski, Nucl. Fusion **37**, 1355 (1997).
- [7] P.C. de Vries *et al.*, Plasma Phys. Control. Fusion **54**, 124032 (2012).
- [8] C. Reux *et al.*, J. Nucl. Mater. **463**, 143 (2015).
- [9] M.N. Rosenbluth *et al.*, in *Proceedings of the 16th International Conference on Fusion Energy, Montreal, 1996* (IAEA, Vienna, 1997), Vol. 2, p. 979.
- [10] S.C. Chiu *et al.*, Nucl. Fusion **38**, 1711 (1998).
- [11] R.W. Harvey *et al.*, Phys. Plasmas **7**, 4590 (2000).
- [12] P. Helander *et al.*, Phys. Plasmas **11**, 5704 (2004).
- [13] H. Smith *et al.*, Phys. Plasmas **12**, 122502 (2005).
- [14] H.M. Smith and E. Verwichte, Phys. Plasmas **15**, 072502 (2008).
- [15] T. Fehér *et al.*, Plasma Phys. Control. Fusion **53**, 035014 (2011).
- [16] A. Stahl *et al.*, Nucl. Fusion **56**, 112009 (2016).
- [17] H. Nuga *et al.*, Phys. Plasmas **23**, 062506 (2016).
- [18] P. Aleynikov and B.N. Breizman, Nucl. Fusion **57**, 046009 (2017).
- [19] J.R. Martín-Solís *et al.*, in *Proceedings of 37th EPS Conference on Plasma Physics* (European Physical Society, Dublin, 2010), Vol. 34A, p. 4.141.
- [20] K.O. Aleynikova *et al.*, in *Proceedings of 40th EPS Conference on Plasma Physics* (European Physical Society, Espoo, 2013), Vol. 37D, European Physical Society, p. O-5.103.
- [21] V.E. Zhogolev and S.V. Konovalov, VANT series Nuclear Fusion **37**, 71 (2014).
- [22] P. Aleynikov *et al.*, in *Proceedings of 25th IAEA Fusion Energy Conference* (IAEA, St. Petersburg, 2014), pp. TH/P3-38.

- [23] J.R. Martín-Solís *et al.*, Phys. Plasmas **22**, 092512 (2015).
- [24] D. Mosher, Phys. Fluids **18**, 846 (1975).
- [25] P. Aleynikov and B.N. Breizman, Phys. Rev. Lett. **114**, 155001 (2015).
- [26] J.R. Martín-Solís *et al.*, Phys. Plasmas **5**, 2370 (1998).
- [27] C.F.F. Karney and N.J. Fisch, Phys. Fluids **29**, 180 (1986).
- [28] C.F.F. Karney, Comput. Phys. Rep. **4**, 183 (1986).
- [29] C. Liu *et al.*, Phys. Plasmas **23**, 010702 (2016).
- [30] C. Liu *et al.*, Plasma Phys. Control. Fusion **59**, 024003 (2017).
- [31] J.R. Martín-Solís *et al.*, Phys. Plasmas **22**, 082503 (2015).
- [32] A.H. Boozer, Nucl. Fusion **57**, 056018 (2017).
- [33] T.C. Hender *et al.*, Nucl. Fusion **47**, S128 (2007).
- [34] J.R. Martín-Solís *et al.*, Nucl. Fusion **57**, 066025 (2017).
- [35] A. Ashkin *et al.*, Phys. Rev. **94**, 357 (1954).
- [36] J.W. Connor and R.J. Hastie, Nucl. Fusion **15**, 415 (1975).
- [37] M. Bakhtiari *et al.*, Phys. Rev. Lett. **94**, 215003 (2005).
- [38] A.H. Boozer, Phys. Plasmas **22**, 032504 (2015).
- [39] P.B. Parks *et al.*, Phys. Plasmas **6**, 2523 (1999).
- [40] H.P. Summers, Atomic Data and Analysis Structure Users Manual Report No. JET-IR 06, JET Joint Undertaking, Abingdon (1994).
- [41] A.A. Solodov and R. Betti, Phys. Plasmas **15**, 042707 (2008).
- [42] D.O. Gericke *et al.*, Phys. Rev. E **65**, 036418 (2002).
- [43] A.E. Kramida and J. Reader, Atom. Data Nucl. Data Tab. **92**, 457 (2006).
- [44] W.R. Leo, *Techniques for Nuclear and Particle Physics Experiments* (Springer-Verlag, Berlin/Heidelberg, 1994).
- [45] M. Bakhtiari *et al.*, Phys. Plasmas **12**, 102503 (2005).
- [46] H.W. Koch and J.W. Motz, Rev. Mod. Phys. **31**, 920 (1959).
- [47] O. Embréus *et al.*, arXiv:1511.03917v1 [physics.plasm-ph].
- [48] O. Embréus, A. Stahl and T. Fülöp, New. J. Phys. **18**, 093023 (2016).
- [49] G. Fussmann, Nucl. Fusion **19**, 327 (1979).
- [50] F. Andersson *et al.*, Phys. Plasmas **8**, 5221 (2001).
- [51] G. Papp *et al.*, Nucl. Fusion **51**, 043004 (2011).
- [52] A. Stahl *et al.*, Phys. Rev. Lett. **114**, 115002 (2015).
- [53] I. Fernández-Gómez *et al.*, Phys. Plasmas **19**, 102504 (2012).
- [54] G.I. Pokol *et al.*, in *Proceedings of 42th EPS Conference on Plasma Physics* (European Physical Society, 2015), Vol. 39E, European Physical Society, p. P-5.169.
- [55] J. Riemann *et al.*, Phys. Plasmas **19**, 012507 (2012).
- [56] V.E. Lukash *et al.*, Nucl. Fusion **47**, 1476 (2007).
- [57] H.P. Summers, Plasma Phys. Control. Fusion **48**, 263 (2006).
- [58] K. Miyamoto, *Plasma Physics for Nucl. Fusion* (Massachusetts Institute for Technology, Cambridge, 1989).
- [59] M. Honda, Jpn. J. Appl. Phys. **52**, 108002 (2013).
- [60] S.P. Hirshman and D.J. Sigmar, Nucl. Fusion **21**, 1079 (1981).
- [61] M. Honda, Phys. Plasmas **21**, 092508 (2014).
- [62] P. Sandquist *et al.*, Phys. Plasmas **13**, 072108 (2006).
- [63] Y. Kawano *et al.*, J. Plasma Fusion Res. **81**, 593 (2005).
- [64] E.M. Hollmann *et al.*, J. Nucl. Mater. **415**, S27 (2011).
- [65] A. Matsuyama *et al.*, Nucl. Fusion **57**, 066038 (2017).
- [66] S.A. Bozhenkov *et al.*, Nucl. Fusion **51**, 083033 (2011).
- [67] P.B. Parks and W. Wu, Nucl. Fusion **54**, 023002 (2014).
- [68] E. Nardon *et al.*, Nucl. Fusion **57**, 016027 (2017).
- [69] V.A. Izzo, Phys. Plasmas **20**, 056107 (2013).
- [70] E. Nardon *et al.*, Plasma Phys. Control. Fusion **59**, 014006 (2017).
- [71] E. Hollmann *et al.*, Phys. Plasmas **22**, 056108 (2015).